The Wendelstein Calar Alto Pixellensing Project (WeCAPP): The M31 Variable Star Catalogue [⋆]

Jürgen Fliri[1⋆⋆], Arno Riffeser[1,2⋆⋆], Stella Seitz[1], and Ralf Bender[1,2]

[1] Universitätssternwarte München, Scheinerstrasse 1, 81679 München

[2] Max-Planck-Institut für Extraterrestrische Physik, Giessenbachstrasse, 85748 Garching

retrieved, accepted: to be inserted later

Abstract. In this paper we present the WeCAPP variable star catalogue towards the bulge of M31. The observations of the WeCAPP microlensing survey (optical R and I bands) during three years (2000-2003) result in a database with unprecedented time coverage for an extragalactic variable star study. We detect 23781 variable sources in a $16.1' \times 16.6'$ field centered on the nucleus of M31. The catalogue of variable stars contains the positions, the periods and the variations in the R and I bands. We classify the variables according to their position in the R-band period-amplitude plane. Three groups can be distinguished; while the first two groups can be mainly associated with Cepheid-like variables (population I Cepheids in group I, type II Cepheids and RV Tauri stars in group II), the third one consists of Long Period Variables (LPVs). We detect 37 RV Tauri stars and 11 RV Tauri candidates which is one of the largest collections of this class of stars to date. The classification scheme is supported by Fourier decomposition of the light curves. Our data shows a correlation of the low-order Fourier coefficients Φ_{21} with Φ_{31} (as defined by Simon & Lee (1981)) for classical Cepheids, as well for type II Cepheids and RV Tauri stars. Correlating our sample of variable stars with the X-ray based catalogues of Kaaret (2002) and Kong et al. (2002) results in 23 and 31 coincidences, 8 of which are M31 globular clusters. The number density of detected variables is clearly not symmetric, which has to be included in the calculations of the expected microlensing event rate towards M31. This asymmetry is due to the enhanced extinction in the spiral arms superimposed on the bulge of M31 which reduces the number of sources to about 60%, if compared to areas of equivalent bulge brightness (without enhanced extinction being present).

Key words. galaxies: individual: M 31 - cosmology: dark matter - stars: variables: general - stars: variables: Cepheids - X-rays: stars

1. Introduction

In the last decade the ongoing microlensing surveys greatly extended our knowledge of variable stars. As the observations of these experiments usually cover a long time span with a good time sampling the resulting datasets are suited perfectly for the study of many different types of variable sources. Lots of the progress in this field therefore resulted from the work of collaborations like MACHO (e.g., Alcock et al. (1995, 1998)), EROS (e.g., Beaulieu et al. (1995); Derue et al. (2001)), OGLE (e.g., Cieslinski et al. (2003); Wray, Eyer & Paczynski (2004)) or MOA (e.g., Noda et al. (2002, 2004)). Numerous publications enlarged the list of known variable stars like Cepheids, RR Lyrae or galactic Long Period Variables (LPVs), but also helped to understand the physical processes dominating these stars.

M31 was surveyed for variable sources since the 1920s starting with the pioneering work of Edwin Hubble. With plates taken at the newly available Mount Wilson telescope Hubble succeeded to resolve Cepheid variables in the outer parts of M31. Using the already established period-luminosity relation, Hubble (1922) was able to determine the distance to M31 to 300 kpc (the difference to the actual value of 780 kpc (Stanek & Garnavich, 1998) is mainly due to an erroneous calibration of the zero-point of the PL-relation and a missing reddening correction) and in this way to reveal the extragalactic nature of the 'Andromeda Nebula'.

Baade & Swope (1963, 1965) continued the work on variable stars in M31 and detected over 400 variables,

---

among them Cepheids and novae. Looking at the relations between period, luminosity, amplitude and frequency they found that the Cepheids resemble the ones in the Milky Way, but seem to be different from those in the Small Magellanic Cloud. Another comprehensive study was performed by the DIRECT project (Kaluzny et al., 1998) who detected and examined Cepheids and Detached Eclipsing Binaries in five fields towards the M31 disk in order to reduce the uncertainties in the distance determination of M31. Unfortunately, the data of a 6th field towards the bulge of M31, which in part overlaps with our surveyed area, remained unpublished.

In the last years Andromeda was target of several microlensing surveys (AGAPE (Ansari et al., 1997), POINT-AGAPE (Auriere et al., 2001), WeCAPP (Riffeser et al., 2001), MEGA (de Jong et al., 2004), SLOTT/AGAPE (Calchi Novati et al., 2002)) looking for compact dark matter in the halo of M31. As by-product of these surveys, catalogues of variable sources start to appear. The work presented in this paper overlaps with the work resulting from the AGAPE (Ansari et al., 2004) and POINT-AGAPE (An et al., 2004) data sets.

Due to our daily stacking scheme of the observations, we are not sensitive to variations and periods smaller than 1.3 days and focus therefore on variations of longer period variables, namely Cepheids, RV Tauri stars, and Long Period Variables (LPVs), i.e. Miras and semi-regular variables. The catalogue is completed by eclipsing binaries, and variables showing eruptive or irregular variations. δ Scuti and RR Lyrae stars show variation amplitudes below our detection limit and will therefore be missed in this study.

The paper is organized as follows. In Sec. 2 we give an overview of the survey, the observations, and data reduction. Sec. 3 deals with the source detection and the derivation of possible periods of the variables. In Secs. 4 and 5, we show the different groups of variable sources detected in the survey. The catalogue of variable stars is presented in Sec. 6 and is correlated with X-ray selected catalogues in Sec. 7. Whereas Sec. 8 summarizes the paper, the appendix deals with the accuracy of the derived periods.

2. The dataset

2.1. Description of the survey

The data presented here result from three years observations of the central part of M31 by the WeCAPP project. We obtained data from the 0.8 m telescope at Wendelstein Observatory (Germany), and from the 1.23 m telescope at Calar Alto Observatory (Spain). At Wendelstein with its field of view (FOV) of $8.3' \times 8.3'$ we selected a field (F1 in the following) along the minor axis of M31 which contains the area with the highest expected rate for pixellensing events (see also Fig. 1 for the location of F1). Observations of this field were accompanied by images of F3, the opposite field along the NW minor axis, taken with a sparser
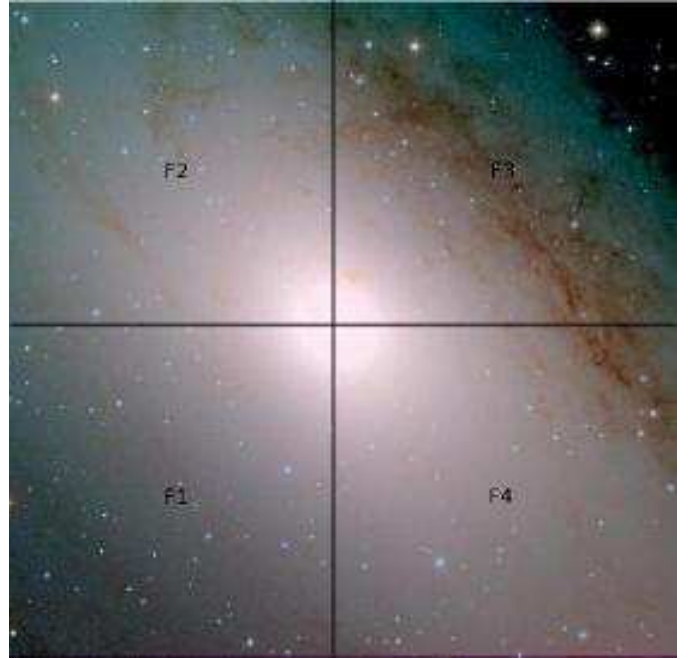

Fig. 1. V-,R-, and I-band composite image of the observed fields F1 to F4, taken at Calar Alto Observatory during the campaign 2000/2001. The black lines mark the positions of fields F1 to F4. The identified variable sources lie within RA(2000): [00h43m25.0s, 00h41m59.9s] and DEC(2000): [41d08′00.1″, 41d24′18.0″].

time sampling. The Calar Alto field covered $17.2' \times 17.2'$ centered on the nucleus of M31. Two quadrants of the field coincided with the maximal lensing field F1 and the opposite field F3. Due to the simultaneous observations we reached a very good time sampling during the observability of M31. Since summer 2002 we are mosaicing fields F1 to F4 with the Wendelstein telescope solely. A composite image (V-, R-, and I-band) of fields F1 to F4 taken at Calar Alto Observatory during the campaign 2000/2001 is shown in Fig. 1. The epochs with data taken for the four fields are shown in Fig. 2.
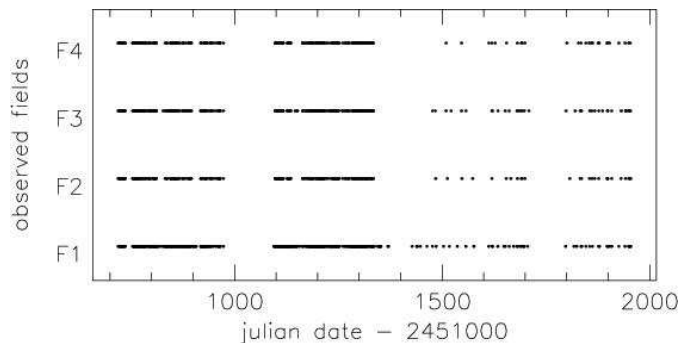

Fig. 2. Distribution of the observations for the four fields. During the first two campaigns we reached a very dense time sampling of the observations. Note that the third and fourth campaign were restricted to Wendelstein Observatory only.

2.2. Instruments and filters

An overview of the cameras and CCDs used in WeCAPP is shown in Table 1. The cameras are a 1K × 1K TEK camera with a pixel size of 0.49″ at Wendelstein and a 2K × 2K SITe camera with a pixel size of 0.5″ at Calar Alto. The observations were carried out in R and I filters close to the Kron-Cousins system. At Wendelstein we used the R ($\lambda \simeq 650\,nm$, $\Delta\lambda \simeq 150\,nm$) and I ($\lambda \simeq 850\,nm$, $\Delta\lambda \simeq 150\,nm$) wavebands. The Calar Alto observations were carried out with the very similar filters, $R(\lambda \simeq 640\,nm$, $\Delta\lambda \simeq 160\,nm)$ and I ($\lambda \simeq 850\,nm$, $\Delta\lambda \simeq 150\,nm$). Despite of the combination of different telescopes, CCDs, and slightly different filter systems we observed no systematic effects in the light curves depending on these parameters (see also Fig. 28 where we show the data obtained at Calar Alto and at Wendelstein separately.)

2.3. Data reduction

The WeCAPP reduction pipeline mupipe will be presented in a future publication (Riffeser, Fliri, & Gössl, 2005, in prep.). mupipe combines all reduction steps from de-biasing of the images until PSF (point-spread-function) photometry and the final measurements of the light-curve in one software package, including full error propagation from the first reduction step to the last (Gössl & Riffeser, 2002):

1. standard CCD reduction including de-biasing, flat-fielding and filtering of cosmic ray events
2. position alignment on a reference grid using a flux conserving interpolation routine
3. photometric alignment of the images
4. restoration of pixels damaged by CCD defects (cold and hot pixels, traps, bad columns) or pixels hit by cosmic ray events
5. stacking of the frames of one epoch (i.e. night) using a weighting scheme to maximize the S/N for point sources
6. matching of the PSF of a high S/N reference frame to the PSF of each stacked frame using our implementation of the image subtraction method developed by Alard & Lupton (1998) and Alard (2000)
7. generation of difference images by subtracting the convolved reference frame from each stacked frame
8. PSF photometry of each pixel in the difference frames using a PSF extracted from the convolved high S/N reference frame
9. extraction of the light curves

A floating chart of the reduction pipeline is shown in Fig. 3. In the last step mupipe returns roughly 4×10^6 pixel light curves together with appropriate errors, each of the light curves representing the time variability of the flux present inside the PSF centered on the particular pixel. The extraction of intrinsic variable sources from these pixel light curves is presented in the next section.
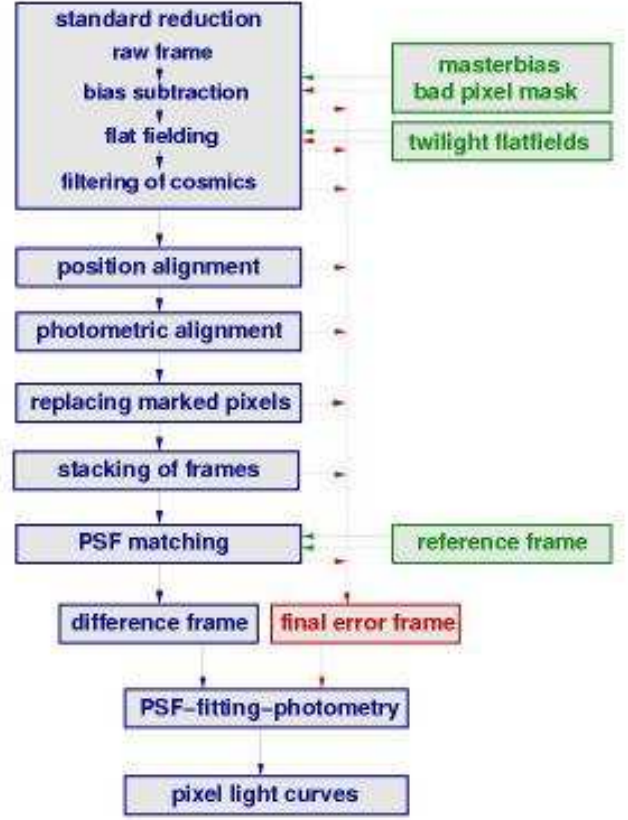

Fig. 3. Floating chart of the WeCAPP reduction pipeline mupipe. The reduction package includes full error propagation for each pixel through all reduction steps. In this way, all data points are properly taken into account in the search for variable sources. The reduction pipeline returns light curves for each pixel in the frame, representing the temporal change of the flux present inside the PSF centered on the particular pixel.

2.4. Astrometry

The astrometric solution was created using the IRAF[1] tasks ccmap and cctran for 92 stars whose positions were taken from the Local Group Survey (LGS, Massey et al. (2001)). The rms of the solution is 0.10″ in declination and 0.12″ in right ascension. The errors of the astrometric solution for the 92 calibration stars are shown in Fig. 4. The coordinates derived here agree perfectly with the one's derived in Riffeser et al. (2001) and Riffeser et al. (2003).

Site	Campaign	CCD	Size	[arcsec/px]	Field [arcmin^2]
We	2000-2003	TEK #1	$1K \times 1K$	0.49	8.3×8.3
CA	2000-2002	SITe2b #17	$2K \times 2K$	0.50	17.2×17.2

Table 1. Properties of the CCD cameras used during WeCAPP at Wendelstein (We) and Calar Alto (CA) Observatories, respectively. Both CCDs have a pixel size of $24\,\mu$m.
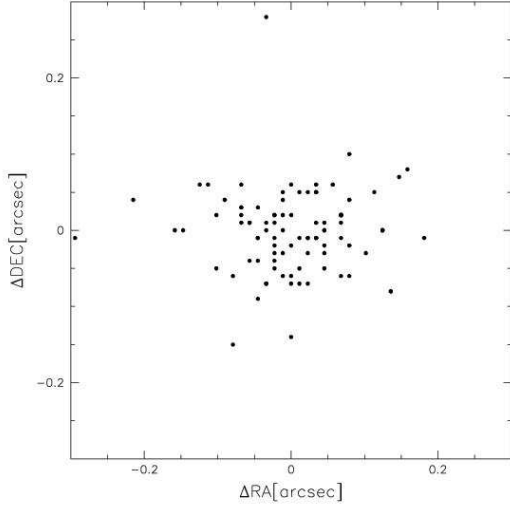

Fig. 4. Errors of the astrometric solution for the calibration stars taken from the LGS survey. The rms is $0.10''$ in declination and $0.12''$ in right ascension.

3. Detection of variable sources

3.1. Selection of the sources

For the selection of the intrinsic variable sources we use the R-band data from the Calar Alto campaigns 2000/2001 and 2001/2002 to create a χ^2_ν variation frame. To get rid of systematic effects induced by the different seeing conditions of each frame we use the following approach. We select a stacked image with roughly the median seeing of the 2000/2001 campaign (about $1.5''$) as master frame and match the PSF of each stacked frame with a smaller PSF to the one of the master frame. In this way we end with difference images for 113 epochs (i.e. 48 % of the epochs with R-band data obtained at Calar Alto) which are used for the detection of the variable sources. For each of the light curves extracted from the PSF$_{1.5}$ difference images we calculate the reduced χ^2_ν deviation from a constant (i.e. zero) baseline fit. The errors entering this calculations are the propagated errors as returned from mupipe. The results are written into a χ^2_ν-frame of the field. The mode of the χ^2_ν-frame is 1.02 which shows the accuracy of the propagated errors (see Fig. 5). Each value ≥ 1.15 is connected to a non-constant, i.e. variable source at the 99.99 % confidence level.

To avoid contamination of the M31 sample with foreground objects we set all pixels in a radius of 5 pixels around the positions of bright foreground stars to zero before detecting the variable sources in the χ^2_ν-frame. We determine the positions of the variable sources using the SExtractor software (Bertin & Arnouts, 1996) for source detection applied on the χ^2_ν-frame. In this way we detect 25571 variable sources in our observed field. Figure 6 shows an extract of the χ^2_ν-frame with the positions of the detected sources marked.

3.2. Period determination

We use an algorithm developed by Lomb (1976) and Scargle (1982) to determine the significance and value of a possible period of the variables sources. The method of Lomb is well suited for this problem as it is able to deal with unevenly sampled data.

The algorithm extracts the power in the first sine and cosine terms for a set of equidistantly spaced frequencies and also yields the significance of the detected peaks in the power spectrum. The Lomb normalized periodogram for N measured data points $h_j = h(t_j)$, $j = 1, ..., N$, taken at epochs t_j is defined by

$$P_N(\omega) = \frac{1}{2\sigma^2} \frac{\left[\sum_j (h_j - \bar{h}) \cos \omega (t_j - \tau)\right]^2}{\sum_j \cos^2 \omega (t_j - \tau)} + \frac{1}{2\sigma^2} \frac{\left[\sum_j (h_j - \bar{h}) \sin \omega (t_j - \tau)\right]^2}{\sum_j \sin^2 \omega (t_j - \tau)} \quad , \quad (1)$$
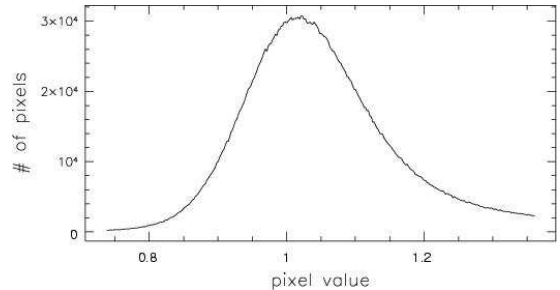

Fig. 5. Histogram of the pixel values measured in the χ^2_ν-frame. The maximum of the distribution of 1.02 reflects the accuracy of the propagated errors.
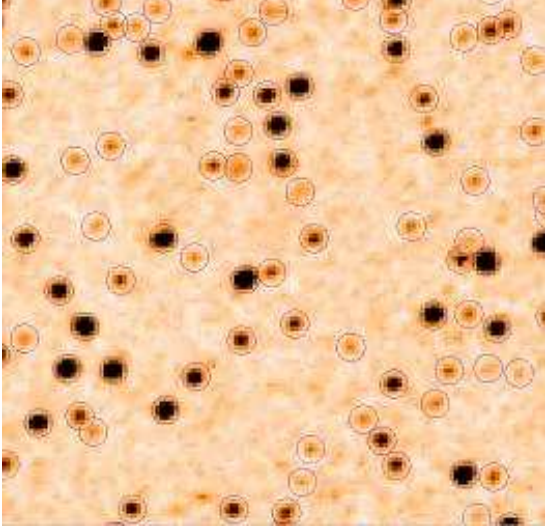
Fig. 6. Extract $(1' \times 1')$ of the χ^2_ν-frame of the over 25000 variable sources detected by the WeCAPP microlensing survey of M31. The circles give the positions of the sources detected by SExtractor. Most of the sources are first identifications, the majority of them being Long Period Variables (LPVs), i.e. Miras and semi-regular variables (see Sec. 4).

where $\omega = 2\pi\nu = \frac{2\pi}{P}$ is the angular frequency for the period P, and the mean $\bar{h}$, the variance σ^2, and the constant τ are defined as follows

$$\bar{h} \equiv \frac{1}{N} \sum_{j=1}^{N} h_j \ , \tag{2}$$

$$\sigma^2 \equiv \frac{1}{N-1} \sum_{j=1}^{N} (h_j - \bar{h})^2 \ , \tag{3}$$

$$\tan(2\omega\tau) \equiv \frac{\sum_j \sin 2\omega t_j}{\sum_j \cos 2\omega t_j} \ . \tag{4}$$

The last definition ensures the power spectrum to be independent on a shift of each t_j by Δt, as τ transforms in that case into $(\tau + \Delta t)$. Lomb (1976) has shown that the evaluation of the periodogram according to Eq. 1 is identical to a linear least-squares fit of the first harmonics

$$F(t) = A \sin \omega t + B \cos \omega t \tag{5}$$

to the data points. In Fig. 7 we show two examples for $P_N(\omega)$, the first one derived from a Cepheid light curve, the second one derived from the light curve of a Long Periodic Variable.

The significance level $P(> z)$ of a peak with amplitude z in the power spectrum is given by

$$P(> z) \equiv 1 - (1 - e^{-z})^M \quad , \tag{6}$$

with $(1 - e^{-z})^M$ being the probability that none of the M tested frequencies shows an amplitude greater than z
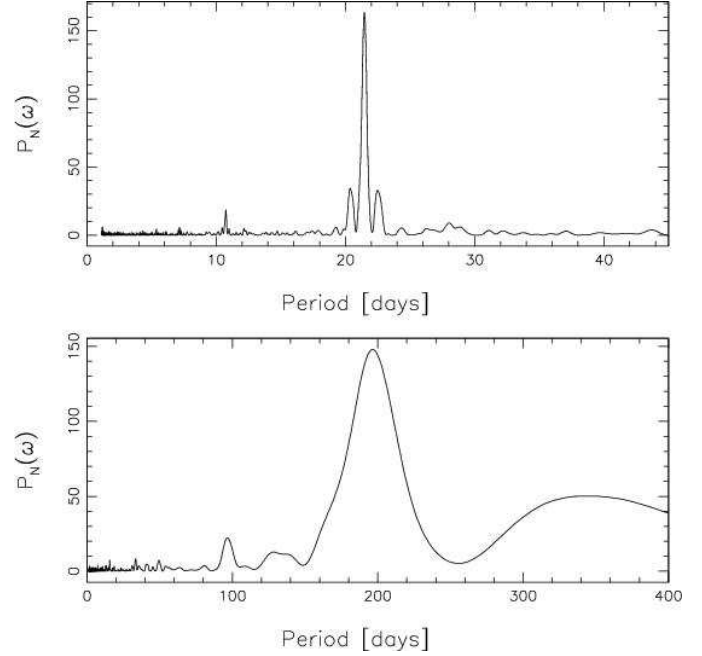

Fig. 7. Two examples of power spectra $P_N(\omega)$ of WeCAPP variables. In the upper panel we show the periodogram for a Cepheid (see also Fig. 24) derived from the R-band data, in the lower panel we show the periodogram for a Long Periodic Variable (see also Fig. 28) derived from the I-band data.

in case of pure Gaussian noise. Horne & Baliunas (1986) showed with extensive Monte Carlo simulations, that the value of M, i.e. the number of independent frequencies does not differ much from the number of data points N, if the data points are not closely clumped.

We use the implementation of the algorithm taken from the Numerical Recipes (Press et al., 1988). Small modifications in the code allow us to search for the different maxima in the power spectrum. The positions and values of the peaks are returned and can be used for further study of the light curves. In this implementation the significance $P(> z)$ is approximated for small values of $P(> z)$ by

$$P(> z) \approx M e^{-z} \quad , \tag{7}$$

where M is a product of the number of data points N and a user supplied value, which determines the high end cut-off of the tested frequencies relative to the Nyquist frequency.

4. The variable sources

4.1. Creating the catalogue

We detect 25571 variable point sources in a $16.1' \times 16.6'$ field centered on the nucleus of M31. As this sample still can contain spurious detections or sources with only a few data points measured in the light curve we apply a couple of cuts which mark different levels of accuracy of
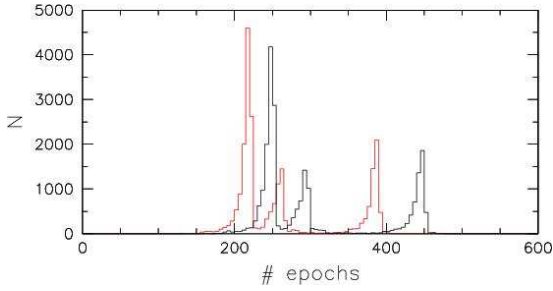
Fig. 8. Histogram of the number of epochs of the level A sources in the $R-$ band (black curve) and I-band (red curve). For sources located in field F1 we usually got data points in the R-band on more than 400 epochs.

the derived periods and the required need for a visual inspection.

As first cut we demand that the light curve comprises at least 40 data points in both filters. All sources which do not pass this criterion are removed from the sample. This reduces the number of variables under inspection to 25316 and defines the **level A sample**. In Fig. 8 we show the histogram of the number of epochs for these sources in the R-band (black curve) and I-band (red curve). The lowest number peaks represent the time sampling present in fields F2 and F4, followed by the peak corresponding to field F3. As F2 and F4 were observed with comparable frequency both fields contribute to the lowest number peak. The last peak with usually more than 400 epochs in the R-band is related to field F1.

As the Lomb algorithm assumes that all data points have the same error (see Eqs. 1 and 3), data points with big error bars or outliers can spoil the period finding process and yield spurious periods. To avoid this we first eliminate in each light curve ten data points with the biggest errors and in a second step five data points with the highest and lowest values, respectively. In doing so, we ensure that we have at least 20 data points in both filters to look for a periodic signal.

We now check the R-band and I-band light curves separately for periodicities. As the color of variable stars usually changes during a cycle combing the two data sets would not result in accurate determinations of the period of the sources. Finally we obtain 25316 variables with determined periods (of any significance level) in both bands.

We regard those periods as real which are the same in both bands inside tight boundaries reflecting the error of the period determination. For periods $P_R < 215$ days we take the theoretical error (see Eq. A.2) resulting from ν_{FWHM} as limit, from 215 days onwards we choose a more conservative constant limit of 30 days, which is increased to 60 days for $P_R > 400$ days. This criterion defines the **level B sample** (20311 objects).

As final cut we select all variables from level B which show a significance level of the period determination of $P(> z) < 10^{-10}$ in R or I and which have a determined R-band period $P_R \leq 450$ days. This final cut reduces the number of sources to 19551 and defines the **level C sam-**

ple with well determined periods. The remaining sources in level B were inspected visually and assigned to the group of regular, irregular, long-variation (period could not be determined because of an incomplete cycle) or miscellaneous variables in the **final catalogue**, or rejected from the sample as spurious detections. Finally, all sources of the level C sample are added automatically to the final catalogue.

For the variables which show deviant periods in R and I we proceed as follows. If the significance level of one of the deviant periods is better than 10^{-15} and at the same time better than the significance in the other band by a factor of 10^{10} we choose the period in the first band and add the variable to the final catalogue. If this is not the case we inspect the light curve visually and decide if one of the periods is the real one, or if the variation is of irregular nature. In this step we also reject the last spurious detections from the sample, the true variables are added to the final catalogue.

4.1.1. Search for eclipsing binaries

By visual inspection of the folded light curves of the Lomb sample we detect 28 eclipsing binary (EB) candidates, amongst them one (semi-)detached system. However, the Lomb algorithm can fail in detecting periods for potential EB systems in M31. As EB light curves, especially the ones of detached systems, show strong power in the higher harmonics, they are not well recovered by Fourier techniques using the first harmonic only. Since some EB candidates therefore could be missed by using the Lomb algorithm alone, we add another step to the search for EBs. We investigate all light curves which were removed in the previous steps once more, however use this time the dedicated transit finding algorithm 'boxfitting' (Kovacs et al., 2002) for the period determination. As Tingley (2003) has shown the boxfitting algorithm is a powerful tool for the detection of eclipsing systems. We implemented the original Fortran code[2] into our detection pipeline and run the algorithm over the mostly noisy light curves which were removed from the sample as spurious detections in the previous steps. In this way we assure to have proper periods for all potential EB candidates present among our variable sources.

Selecting all light curves with a reasonable signal detection efficiency (SDE, Kovacs et al. (2002)) SDE > 6, periods $P > 1.30$ days, and rejecting periods between 1.95 days and 2.05 days (to avoid to pick up aliasing periods) results in an additional sample of 155 light curves. Visual inspection of the folded light curves finally yields 3 additional candidates for (semi-)detached eclipsing binary systems.

In Fig. 9 we show the distribution of periods of the 31 EB candidates in the upper panel. The 4 (semi-)detached systems populate the low period area up to a period of 7 days whereas the candidate contact systems generally have

---

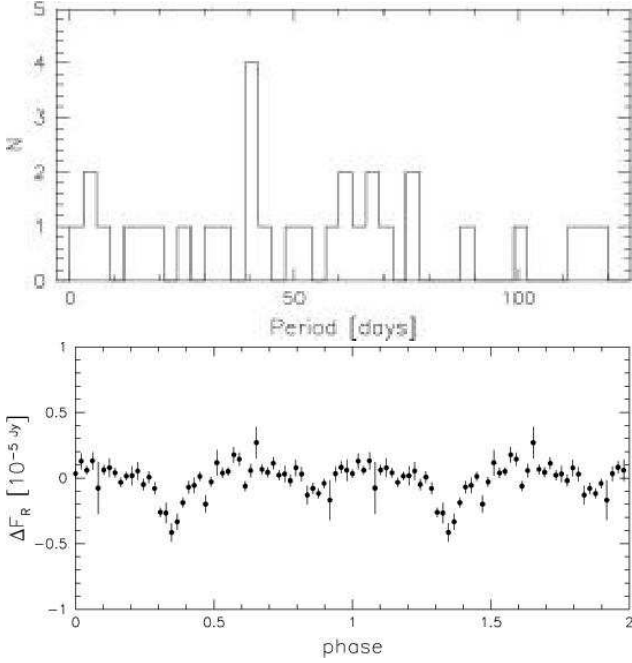[2] http://www.konkoly.hu/staff/kovacs.html

Fig. 9. Top panel: Histogram of the periods of the 31 eclipsing binary candidates. The 4 (semi-)detached systems populate the low period area up to a period of 7 days whereas the candidate contact systems generally have longer periods. Bottom panel: binned R-band light curve of a semi-detached system in the phase representation. The system has a R-band period of 7.08 days.
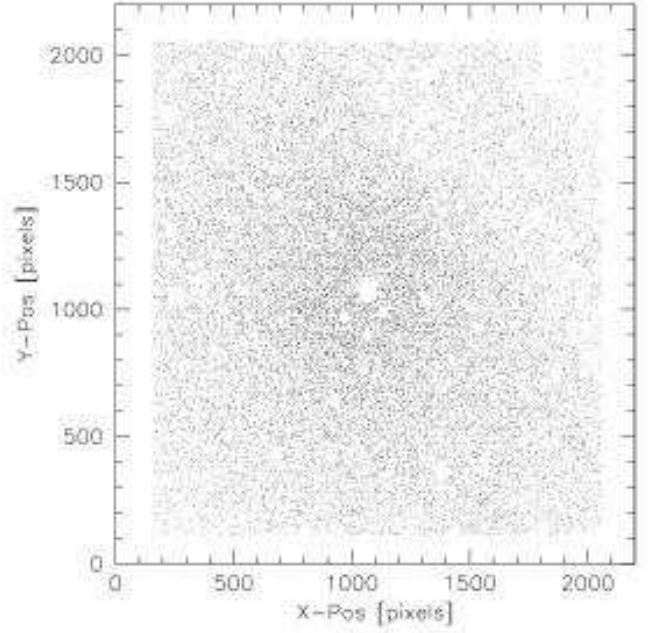
Fig. 10. Positions of the 23781 variable sources of the final catalogue. Blank regions are connected to to saturated parts of the frame or to eliminated foreground stars. Incompleteness induced by crowding in the center and the influence of the enhanced extinction connected with the spiral arms superimposed over the M31 bulge are clearly visible (see also Fig. 12).
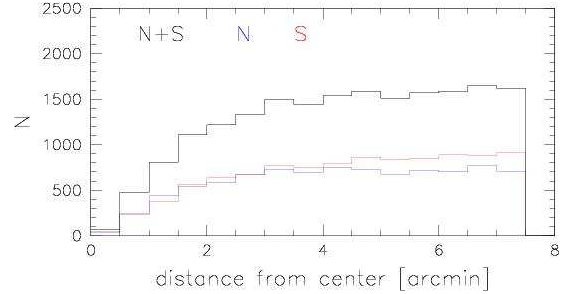
longer periods. In the bottom panel we show the binned R-band light curve of a semi-detached system in the phase representation. The system was detected using the Lomb algorithm and has a R-band period of 7.08 days.

4.2. Number counts and asymmetry

In Fig. 10 we show the positions of the variables from the final catalogue, which suggests a connection of the enhanced extinction in M31's spiral arms and the depletion of sources in certain regions in the northern part of the bulge (field F3). This depletion is also evident from number counts of the sources in the northern and southern hemisphere of M31 (see Fig.11).

We are calculating the number density of variable sources by summing up all variables in 100×100 pixel $[50'' \times 50'']$ bins. In the resulting density map (Fig. 12) the spiral arms are clearly visible. A comparison of the number densities at equivalent positions in the M31 bulge, one in the dust lane of the spiral arms, the other one in the opposite hemisphere, shows a reduction to about 60% relative to the part with no strong extinction.

To examine this subject further we compare the positions map (see Fig. 10) with an extinction map of our field. In Fig. 13 we plot the positions of the sources on top of the R-band extinction map, which we derived from the V- and R-band frames taken by the LGS survey in the following way:

Fig. 11. Number counts of sources of the catalogue as function of the distance to the center of M31. Black: all sources. Blue: sources in the northern hemisphere of M31. Red: sources in the southern hemisphere of M31. Clearly visible is the asymmetry of the detected sources due to the enhanced disk-extinction in the northern part. The low number of sources near the center is due to incompleteness induced by crowding and saturated parts in the frames.

We start from the relation between the color excess $E(V - R)$ and the extinction A_R in the R-band ($a \approx 3$, see Binney & Merrifield (1988))

$$A_R = a\, E(V - R) \qquad (8)$$

With the non-reddened magnitudes $M_{R,0}, M_{V,0}$ and reddened counterparts $M_{R,r}, M_{V,r}$ this writes as

$$M_{R,r} - M_{R,0} = a\, [(M_{V,r} - M_{R,r}) - (M_{V,0} - M_{R,0})] \ . \quad (9)$$
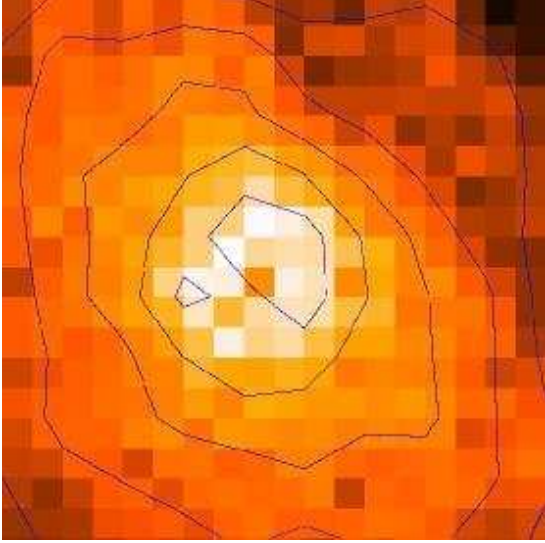
Fig. 12. Number density of variable sources by summing up all variables in 100×100 pixel $[50'' \times 50'']$ bins. To avoid effects induced by the border of the frame we only use pixels in the region [200:2000,200:2000]. The contour levels are 1, 2, 3, 4 and 5 $\times 10^{-2}$ [arcsec^{-2}], respectively. The spiral arm is clearly visible. Due to extinction in the dust lanes the number density reduces to about 60% when compared to equivalent regions without strong dust features being present. The regions with underdensities near the center are due to saturated parts in the frame with no variable sources detected.

The transformation to fluxes $F_{i,j}$ ($i = R, V; j = 0, r$) yields

$$F_{R,0} = F_{R,r} \left(\frac{F_{R,r}}{F_{V,r}}\right)^a \left(\frac{F_{V,0}}{F_{R,0}}\right)^a \quad . \tag{10}$$

If we now suppose that the intrinsic stellar population gradients are negligible over the field we can set $\left(\frac{F_{V,0}}{F_{R,0}}\right) \approx constant$, which is not exactly true but a valid approximation for our purposes.

Using this assumption we finally obtain a relation for $F_{R,0}$

$$F_{R,0} = \frac{F_{R,r}^{1+a}}{F_{V,r}^a} \left(\frac{F_{V,0}}{F_{R,0}}\right)^a \quad , \tag{11}$$

which can be used to calculate the extinction ext_R in the R-band

$$ext_R = -2.5 \log\left(\frac{F_{R,r}}{F_{R,0}}\right) \quad . \tag{12}$$

For the intrinsic color $(V - R)_0$ required in the calculation we use the theoretical value $(V - R)_0 = 0.63$, assuming the bulge to be a 12 Gyr old SSP of $2Z_\odot$ metalicity (C. Maraston, priv. comm.). Figure 13 shows the resulting extinction map: indeed under-dense variable source regions coincide with high extinction regions.
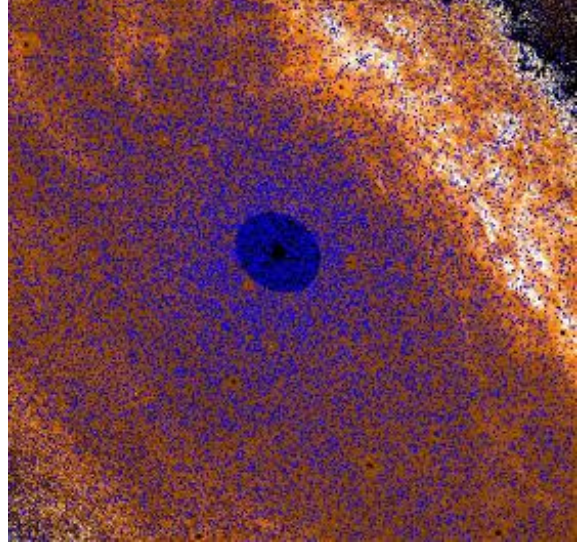

Fig. 13. R-band extinction map of the M31 field. White areas correspond to high extinction values. The extinction in the R-band was derived using the V- and R-band images taken from the LGS survey (Massey et al., 2001). Overplotted are the positions of the catalogue variables (blue dots). In the central regions the extinction map could not be calculated due to saturation in the original LGS frames.

Finally we compare the number densities of sources present in our catalogue with theoretical predictions. According to Renzini (1998) the number of LPVs per integrated 10^5 bolometric luminosities is equal to 0.5. Renzini (1998) uses a slightly older (15 Gyrs) and less metal-rich (1 $Z_\odot$) bulge if compared to the model used for the calculation of the extinction frame. With the small bulge decomposition of Kent (1989) and under the assumption that the LPVs are present in the bulge only, we derive the expected number densities of LPVs and show it in Fig. 14. The agreement with the detected number densities is good in the outer parts of the field. Towards the center we suffer from incompleteness due to enhanced noise on the one hand and crowding of the sources on the other hand.

4.3. Classification scheme

As practically all of the detected sources are unresolved in the original frames we are neither able to put the sources in the color-magnitude plane and to construct a color-magnitude diagram, nor to derive period-luminosity relations for the different classes. The available parameters for establishing a classification scheme are therefore reduced, leaving the period, its significance, the amplitude of the variation, its (flux excess)-color, and finally the light curve shape as classification parameters. The light curve shape is of particular interest as it can be described mathematically and parameterized in terms of the parameters resulting from low order Fourier fits to the data. For classical Cepheids the Fourier parameters show a progression
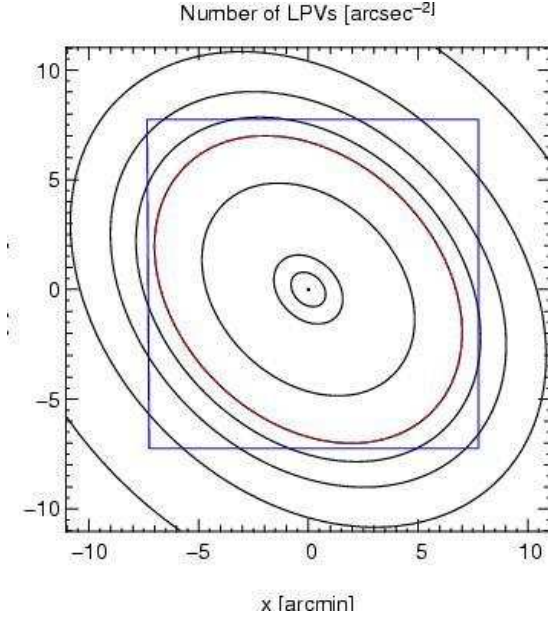
Fig. 14. Theoretical expected number densities of LPVs according to Renzini (1998) calculated with the small bulge decomposition of Kent (1989) . The field is centered on the nucleus of M31, north is on top, east is on the left of the diagram. The WeCAPP field for which we calculated the number density in Fig. 12 is shown by blue lines. Contour levels are 1, 2, 3, 4 and 5 $\times 10^{-2}$, 0.1, 0.5, 1, 5 and 10 sources [arcsec^{-2}]. The red line marks the 5×10^{-2} contour level.
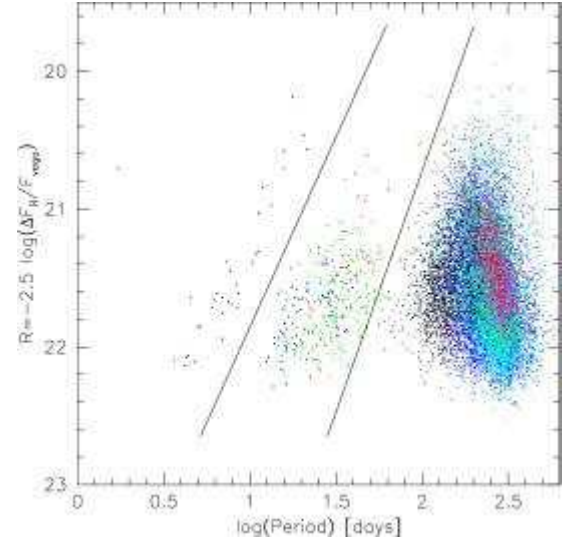

Fig. 15. Period-amplitude relation in the R-band for the catalogue sources (eclipsing binaries, irregular, long-variation, and miscellaneous variables excluded). The amplitudes were transformed in magnitudes using the R-band fluxes of Vega. Note that these magnitudes reflect the flux difference only and are not the real variation magnitude of a single star. In this diagram three populations are visible. The black lines show the defining relations (from left to right) for group I (population I Cepheids: black dots), group II (type II Cepheids: blue dots, RV Tauri stars: red dots, RV Tauri candidates: open magenta circles, SR variables: green dots), and group III (LPVs). For the RV Tauri stars and candidates we use the single or fundamental period (minimum to minimum). The sources in group III are color coded according to the significance of the I-band period as returned by the Lomb algorithm (low significance: black $\rightarrow$ blue $\rightarrow$ red: high significance).

with the period of the variation, echoing the well-known 'Hertzsprung progression' (Hertzsprug, 1924) of the light curve shape with period. For type II Cepheids likewise correlations have already been found; the analysis of the RV Tauri stars in our sample reveals a correlation between different phase parameters. Fourier decomposition of the light curves therefore is a powerful method to support the classification of Cepheid-like variables and discriminate them from other type of variables. On first ground our classification scheme is based on the position of the stars in the R-band period-amplitude plane. For certain groups of stars we refine and check our classification by using the Fourier parameters of the fits to the light curves.

4.3.1. Period-amplitude-relations

The amplitudes ΔF_R and ΔF_I of the variation in the R-band and I-band are determined as half the difference of the maximum to the minimum of the light curves. As we calculate the amplitudes after having eliminated data points with the largest error bars and biggest flux differences this amplitudes act as a lower limit only, but can be regarded as a robust measurement of the variation amplitude. The amplitudes were transformed in magnitudes using the R- and I-band fluxes of Vega taken from Binney & Merrifield (1988). Note that these magnitudes

reflect the flux difference on the frame only, and are not the real variation magnitudes of a single star.

Figure 15 shows the relation between the logarithm of the period and the logarithm of the amplitude ΔF_R (i.e. the variation magnitude as measured in the frame) for the sources of the final catalogue. Three different groups can be distinguished in this diagram:

– Group I has periods between 1.7 and 21.5 days, there seems to be a correlation of the period and the amplitude of the variation in a sense that bigger periods show larger amplitudes. We require $-2.5 \log(\Delta F_R/F_{\mathrm{Vega}}) < 23.1 - 2.76 \, (\log P_R - 0.55)$ for sources belonging to this group. This relation as well as the dividing relation for group II sources is shown as black line in Fig. 15. These stars are most likely connected to the disk, as their light curves and the period regime are connected to Cepheids of type I which belong to a young population.
– Group II has periods in the range between 12 and about 140 days. Also in this group the period and the variation amplitude are correlated, whereas the se-

quence for the group II stars lies at fainter magnitudes than the one of the group I stars. The defining relations for this group are given by $-2.5 \log(\Delta F_R/F_{\text{Vega}}) > 23.1 - 2.76\,(\log P_R - 0.55)$ and $-2.5 \log(\Delta F_R/F_{\text{Vega}}) < 23.0 - 3.5\,(\log P_R - 1.35)$. Group II stars most likely belong to the old spheroid population; RV Tauri stars, type II Cepheids and the low period tail of the semi-regular (SR) stars are found in this group.

– The bulk of the detected variables finally belongs to group III, variables with periods longer than about 50 days. For this group no clear correlation between the amplitude and the period can be seen. All sources with $-2.5 \log(\Delta F_R/F_{\text{Vega}}) > 23.0 - 3.5\,(\log P_R - 1.35)$ belong to this group.

4.3.2. Fourier fits

We fitted truncated Fourier series of the form

$$C + A_0 \Sigma_{i=1}^{N} A_i \cos(i\omega(t - t_0) + \Phi_i) \tag{13}$$

to the R-band light curves of groups I and II. C defines the baseline of the fit, A_0 reflects the overall amplitude of the light curve, and A_i and Φ_i define the amplitudes and phases of the different harmonics. The periods entering the fit are the periods returned by the Lomb algorithm. A fitting order of $N = 5$ leads to acceptable fits to the data.

Simon & Lee (1981) were the first to calculate amplitude ratios of the form $R_{ij} = A_i/A_j$ and phase differences $\Phi_{ij} = \Phi_i - i\Phi_j$ of the parameters of the different harmonics. Since for classical Cepheids both definitions show a progression with the period as well as a correlation among one another, Fourier analysis proved to be an excellent diagnostic to examine the pulsation properties of these stars. Fourier analysis therefore was widely used in the past to examine Cepheids (e.g., Simon & Moffett (1986), Alcock et al. (1999)), particularly to distinguish between fundamental and first overtone pulsators (e.g., Antonello & Poretti (1986), Beaulieu et al. (1995)).

5. Classes of variables

5.1. Group I and II - Cepheid-like variables

Groups I and II are populated by Cepheid-like variables (population I Cepheids in group I, type II Cepheids and RV Tauri stars in group II), and the small period tail of semi-regular variable stars, which start to contribute at periods from about 16 days onwards.

5.1.1. Population I Cepheids

Classical Cepheids are relatively young, intermediate mass population I stars. They pulsate in the fundamental mode which discriminates them from s-Cepheids, which are believed to pulsate in the first overtone. Both groups of population I stars have distinctive light curves, the classical showing skewed, the s-type showing smooth sinusoidal variations.
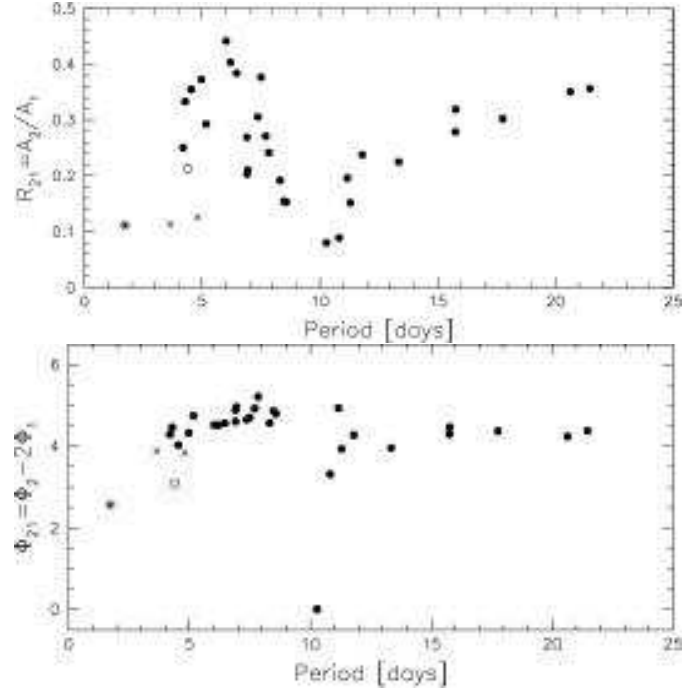

Fig. 16. Amplitude ratio $R_{21} = A_2/A_1$ (upper panel) and phase difference $\Phi_{21} = \Phi_2 - 2\Phi_1$ (bottom panel) determined from the R-band data for the population I Cepheids (group I) plotted against the period. The ratio and phase difference drop as the periods approach the resonance $P_2/P_0 \approx 0.5$ at about 10 days and rise again afterwards. The R_{21} value classifies 29 of the detected Cepheids as fundamental mode pulsators (closed circles), whereas 2 are overtone pulsators (crosses). One of the Cepheids falls of the fundamental mode sequence in the phase difference diagram. Following Beaulieu et al. (1995) we classify this source as intermediate type Cepheid (open circle). The beat Cepheid candidate for which we used the dominant period (presumably the first overtone) in the analysis is marked with an asterisk.

We detect 33 population I Cepheids in our sample. To check whether our classification is correct and if there are first overtone pulsators (s-Cepheids) amongst the detected Cepheids we fitted truncated Fourier series (see Sec. 4.3.2) to the light curves of group I. Figure 16 shows the characteristic progression of the Fourier parameters with the period of the light curve for the classical Cepheids: as the amplitude ratio R_{21} between the first and second harmonic drops the corresponding phase difference shows a mild rise. The amplitude ratio R_{21} declines until a period of about 10 days is reached, and then starts to rise again. Due to the suppression of the second harmonic the Cepheid light curves in the vicinity of this period look quite sinusoidal. Figure 16 shows, that the the minimum of R_{21} is connected to a dramatic change of Φ_{21}. Generally it is believed that this change is connected to the resonance between the fundamental mode and the second overtone $P_2/P_0 \approx 0.5$ (e.g., Simon & Moffett (1986)).
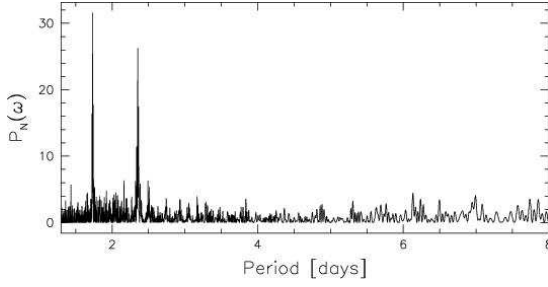
Fig. 17. Power spectrum of the beat Cepheid candidate in the R-band. The two peaks in the spectrum correspond to periods of 1.73 days and 2.35 days.

First overtone pulsators can be detected using the amplitude ratio R_{21}, as s-Cepheids showing smaller values than their fundamental mode counterparts. Following Beaulieu et al. (1995) we demand $R_{21} < 0.3$ for $P < 3$ days and $R_{21} < 0.2$ for $3 \leq P < 5.5$ days for the Cepheids to be classified as first overtone pulsators. Using this criterion we identify 2 first overtone pulsators in our sample. One source with a R_{21} value close to the border to the s-Cepheids falls of the fundamental mode sequence in the phase difference diagram. Following Beaulieu et al. (1995) we classify this source as intermediate Cepheid.

One source is clearly separated from the Cepheid relation in the period-amplitude plane (see Fig. 15). This variable shows Cepheid like variations which are modulated by a period of 208 days in R. The modulation is most likely due to another variable source inside the PSF. Fourier decomposition of the R-band data shows that the source has two excited periods, 1.73 days and 2.35 days, besides the subdominant modulation of the light curve. In Fig. 17 we show the power spectrum of this source. The two periods would classify the source as a beat Cepheid, the first one detected in M31. Beat Cepheids are a rare sub-class of Cepheids in which two pulsation modes are excited simultaneously. The ratio of the two periods $P_{short}/P_{long} \approx 0.73$ makes it likely that we see a fundamental mode / first overtone (F/1H) pulsator, if the Cepheid hypothesis for this source is confirmed. For F/1H beat Cepheids the first overtone should be the dominant mode, which is fulfilled for our candidate. Interestingly, the position in the (P_1/P_0) - $\log (P_0)$ diagram would place this beat Cepheid on a sequence defined by the SMC beat Cepheids of Beaulieu et al. (1997), well above the relations for the LMC and the Galaxy. This would point to a Cepheid in M31 of approximately the same metal content by mass as the SMC beat Cepheids. The object is resolved in our reference image and is also classified as a star (261262) in the Haiman et al. (1994) catalogue. Additionally it was detected in X-rays and appears in the Kong et al. (2002) catalogue (J004301.8+411726, see also Table 4).

In addition to the beat Cepheid there is another peculiar source in group I which remains unclassified at this stage. It shows two periods of 6.95 days and 20.5 days. We will further investigate that object, together with the beat Cepheid candidate, and also present a more detailed description of the Fourier parameters of group I stars in a future publication.

5.1.2. Type II Cepheids and RV Tauri stars

Type II Cepheids are low-mass population II variables which follow a period luminosity relation about 1.5 mag below the classical Cepheid relation. They are found in old populations like globular clusters, the halo or the bulge. Type II Cepheids with periods less than 5 days are also called BL Her or CVB stars, whereas type II Cepheids with periods between 10 and 20 days are often referred as W Virgini stars. At the upper period limit often a period doubling can be observed in the light curves. An approximate period limit of about 20 days (Alcock et al., 1998) separates type II Cepheids from RV Tauri stars which share the same light curve, and often also the same chemical and dynamical characteristics (Fokin, 2001). RV Tauri stars can be recognized by a typical double-wave light curve with alternating deep and shallow minima, their semi-periods (minimum to minimum) ranging from 20 to over 50 days. The current understanding places RV Tauri stars at the end of stellar evolution. After leaving the Asymptotic Giant Branch (AGB, Iben & Renzini (1983)) they move left in the HR-diagram entering the instability strip at high luminosities. For a recent review on population II Cepheids and related stars see Wallerstein (2002). A comprehensive collection of type II Cepheids and RV Tauri stars detected in the LMC by the MACHO collaboration can be found in Alcock et al. (1998).

We detect 37 RV Tauri stars and 11 RV Tauri candidates which makes this catalogue to one of the biggest collections of RV Tauris to date. The light curves show the typical alternation of deep and shallow minima, the second maximum being fainter than the first one, although for a few sources this latter difference is rather marginal. The light curve shape can be divided into two groups, one resembling the *'flat-topped'* Cepheid II shape (see Fig. 26), the other one showing sinusoidal variations. To avoid a mis-classification of the sinusoidal light curves of RV Tauri stars with the not too different light curves of β-Lyrae eclipsing binaries, we extract the phase difference between the second and the fourth harmonic from Fourier fits to the light curves. According to Szymanski, Kubiak, & Udalski (2001) these two phases should be strongly coupled for sinusoidal contact systems, yielding $\Delta \Phi = \Phi_4 - 2\Phi_2 = 0$ (M. Szymanski, priv.comm.). For pulsating stars the correlation is much weaker. 5 of our RV Tauri candidates with sinusoidal light curves have a $\Delta \Phi$ which is within 1-σ compatible with 0 (or equivalently 2π), another 6 lie within 3-σ. We classify all 11 RV Tauris whose $\Delta \Phi$ values are within 3-σ compatible with 0 as RV Tauri candidates, the remaining 37 sources as RV Tauri stars.

Using the fundamental period (minimum to minimum) for the Fourier extension of the RV Tauri sources yields rel-
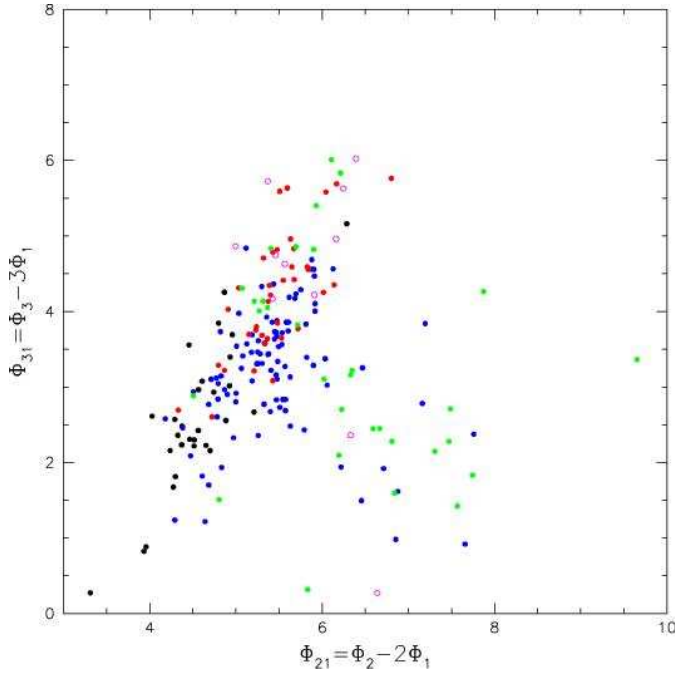
Fig. 18. Phase differences $\Phi_{ij} = \Phi_i - i\,\Phi_j$ as determined from the R-band data plotted against each other. Black dots: population I Cepheids (group I), blue dots: type II Cepheids (group II), red dots: RV Tauri stars (group II), open magenta circles: RV Tauri candidates (group II). As green dots we show the LMC type II Cepheids and RV Tauri stars from Alcock et al. (1998), which fall on the sequences of the WeCAPP sources. For the RV Tauri stars we use the formal period in the analysis. The classical Cepheids show a clear correlation of the two parameters, but also for the type II Cepheids and the RV Tauri stars both phase differences are correlated. The sequences of RV Tauri stars and type II Cepheids overlap, making the RV Tauri sequence to an extension of the Cepheid II sequence. This favors the close connection between these two types of stars.

atively bad fits and subsequently more uncertain Fourier parameters. We therefore use the formal period in the analysis which yields a more appropriate description of the data, better fits, and more reliable Fourier parameters. In Fig. 18 we show a 'phase-phase' diagram as a further result of the Fourier analysis of the RV Tauri and candidate RV Tauri light curves. The phase differences Φ_{31} and Φ_{21} correlate for the RV Tauri light curves (red dots) showing that these sources form a homogeneous group of stars. Also the RV Tauri candidates (magenta open circles) follow the relation supporting the RV Tauri nature of these stars. Furthermore we show the detected type II Cepheids as blue dots in this figure. The sequences of RV Tauri stars and type II Cepheids overlap, making the RV Tauri sequence to an extension of the Cepheid sequence at higher periods. This supports the close connection between RV Tauri stars and type II Cepheids. In fact, Alcock et al. (1998) showed that a single period-luminosity-color relationship describes both the type II Cepheids and RV Tauri
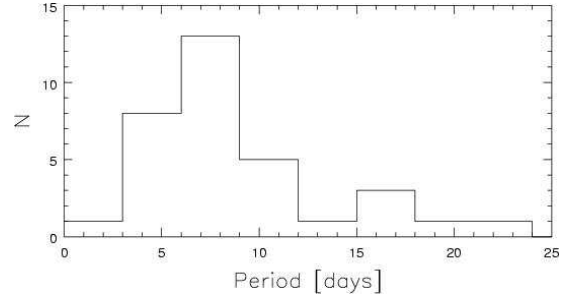

Fig. 19. Histogram of the periods of the Cepheid variables in group I.

stars in the LMC. We show the phase parameters for the stars presented in this study as green dots in Fig. 17. For this purpose we re-analyzed the light curves taken from the MACHO project database[3] and used the formal period to derive the Fourier parameters. Two stars with an uncertain classification were rejected from the analysis. The LMC variables lie on the sequence of the WeCAPP RV Tauri and Cepheid II stars, supporting our classification of the variables of group II. We will present a more thorough discussion of the Fourier parameters of the Cepheid-like variables in group I and II in a future publication.

The period range of the 93 type II Cepheids extends to periods larger than the approximate limit of about 20 days as proposed by Alcock et al. (1998). There is still the possibility that some of these long period Cepheids are in reality RV Tauri stars, since noise in the light curves can prevent us to detect the alternation of deep and shallow maxima as required for the assignment of the variable as a RV Tauri candidate or star. The majority of the light curves of this type of variables are of '*flat-topped*' shape (Kwee, 1967) with relatively long and flat maxima. As already mentioned, the light curves of type II Cepheids show a progression of the phase differences and occupy distinct places in Fourier space. The sample of type II Cepheids outnumbers the sample of population I Cepheids by about a factor of three. As the type II Cepheids trace the old bulge population this is not unexpected, even when taking into account their smaller brightness (at the same period) if compared to population I Cepheids. The population I Cepheids, more massive and younger than the type II Cepheids, are typical members of the M31 disk population, which is superimposed to the M31 bulge.

The third constituent of the group II sources are small period semi-regular variables which contribute from periods about 16 days onwards. The Fourier analysis of the light curves shows no correlations of the amplitude ratios or phase differences with period. Also phase-phase diagrams do not reveal a correlation of the phase parameters.

In Fig. 19 we give the period distribution of the population I Cepheids, whereas Fig. 20 shows the distribution of periods for variables belonging to group II. In red, magenta, blue, and green we present the distribution for the
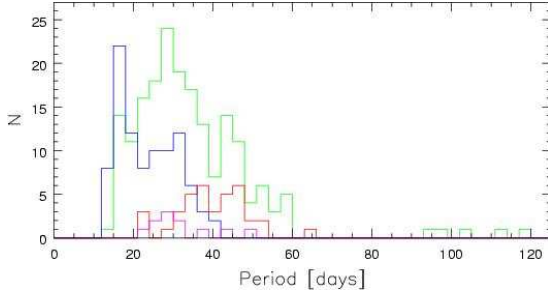
---

[3]   http://wwwmacho.mcmaster.ca/Data/MachoData.html

Fig. 20. Histogram of the periods of variables belonging to group II. We show the distributions for type II Cepheids (blue line), RV Tauri stars (red line), RV Tauri candidates (magenta line) and the semi-regular stars (green line). For the RV Tauri stars and candidates we use the single or fundamental period (minimum to minimum).

RV Tauri stars, RV Tauri candidates, type II Cepheids, and semi-regular variables.

5.2. Group III - LPVs

Group III consists of Long Period Variables (LPVs), i.e. Mira and semi-regular variable stars. LPVs are members of the AGB which marks the final stage of the stellar evolution for intermediate mass stars with masses between 0.5 and 8 $M_\odot$. These stars evolve from the main sequence and populate the red giant branch up to a maximum luminosity at the TRGB (tip of the red giant branch). After ignition of helium core burning they drop in luminosity and form the horizontal branch. At the end of this stadium the luminosity again is rising as the stars evolve upwards the AGB. This evolution sequence is characterized by pulsation and extensive mass loss.

LPVs are a very promising tool for various astrophysical questions. They follow tight period-luminosity relations in the near-IR (especially the K-band) (Feast et al., 1989; Wood, 2000; Feast et al., 2002) which makes them excellent galactic and extragalactic distance estimators. They are furthermore good indicators of the parent population to which they belong, as there exists a dependence of the luminosity (hence period) of Miras on the age. Longer period Miras should have higher mass progenitors and therefore belong to a younger population. LPVs are historically separated in two main groups: i) Miras with regular variations, periods between 80 and 1000 days and an amplitude of the variation in the V-band of more than 2.5 mag; ii) semi-regulars (SR) with less regular variations, smaller periods and a V-band variation smaller than 2.5 mag. Semi-regulars are dived in two groups, SRas with more regular variations and SRbs with variations less regular.

Recently Lebzelter et al. (2002) proposed a new classification scheme less dependent on this kind of artificial division and used it for the AGAPEROS survey of variable red stars towards the Magellanic Clouds. Their classification is based on the regularity of the variation alone,
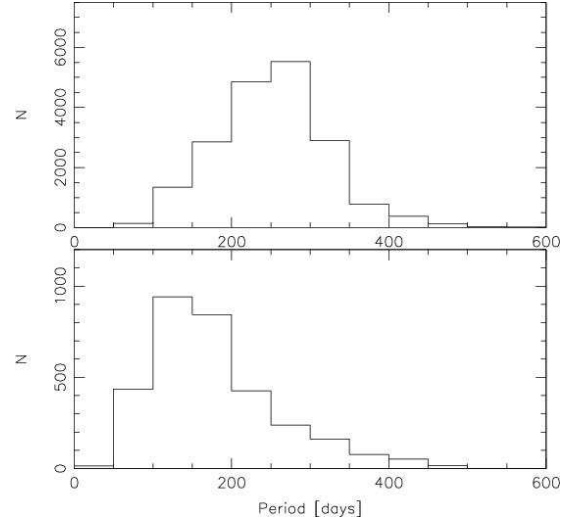

Fig. 21. Distribution of the periods of LPVs in the bulge of M31 detected by the WeCAPP project. Top: class i - regular and semi-regular variables (significance level $P(> z) < 10^{-20}$ in R or I). Bottom: class ii - irregular variables (significance level $P(> z) \geq 10^{-20}$ in R and I). Only irregulars selected by the significance cut are shown. Note that the distribution for the sources classified as irregular variables is of qualitative nature only as the periods for these sources are not well determined. In general irregular variables show smaller 'periods' than the group of regular and semi-regular variables.

providing three classes of stars: i) LPVs with regular variation ii) LPVs with semi-regular variation iii) LPVs with irregular variation. No cuts in amplitude were applied, therefore class i contains members of the classical Mira group as well as members of the SRa type of objects.

We modify this classification scheme for our purposes and define a significance cut of 10^{-20} according to the period finding algorithm in R or I for the division of our sample of LPVs in classes i (regular and semi-regular) and ii (irregular). Class ii coincides with the class of irregular stars introduced in Sec. 4. Because of the non-linear dependence of the significance on the S/N of the light curve (see also discussion below) we abandon to invent an automatic cut for the division into semi-regular and regular variations. The cut at 10^{-20} is somewhat subjective as also stars with semi-regular, but low S/N light curves are classified as irregular, as the low S/N prevents the period to be determined with better significance. On the other hand this cut ensures that most of the irregular light curves are classified in the right way. The histograms of the periods for the irregular and the regular/semi-regular sample of LPVs are shown in Fig. 21. The irregular variables show in the mean smaller 'periods' as the group of regular or semi-regular variables. Note, that this statement is of qualitative nature only, as the periods for these sources are not well determined.

We have color coded the LPVs in Fig. 15 according to the significance of the I-band period. The slope of the
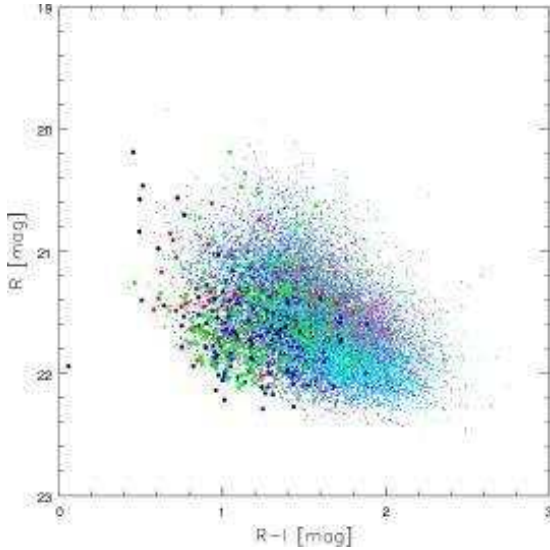
Fig. 22. Variation color $R - I$ shown as a function of the R-band variation magnitude. The sources of groups I and II are shown as big closed circles, the sources of group III as small closed circles. The color coding is the same as in Fig. 15, i.e. the LPVs are again color coded according to the significance of the I-band period. The sources in group I and II as a whole show bluer variations than the LPVs in group III. The significance of the I-band period rises for brighter R variation magnitudes and redder variation colors. This is a result of the higher S/N of the I-band light curves, but can in part also be attributed to the enhanced regularity of the light curves.

variation magnitude-period relation changes from slightly positive for the low significance tail (black dots) to negative for the sources with intermediate and high significant periods (green and red dots). The same trend can be seen in Fig. 22, which shows the variation color $R - I$ as a function of the R-band variation magnitude. The significance of the I-band period rises for brighter R variation magnitudes and redder variation colors. The differences in the significance of the LPV I-band periods therefore is a result of the different S/N of the I-band light curves (rising S/N in I due to higher $R - I$ values), but can in part be also attributed to different stages of regularity in the light curves. Figure 23 finally shows the variation color $R - I$ as function of the period of the variable sources. The variation of the LPVs gets redder with increasing period, and at the same time shows more significant periods.

6. The Catalogue

The final catalogue comprises 23781 entries with group I containing one beat Cepheid candidate, 2 s-Cepheids, one Cepheid of intermediate type, and 29 classical Cepheids pulsating in the fundamental mode. One further group I source which remains unclassified in this catalogue shows two periods.

Group II comprises 93 type II Cepheids, 37 RV Tauri stars, 11 RV Tauri candidates, and 193 low period semi-
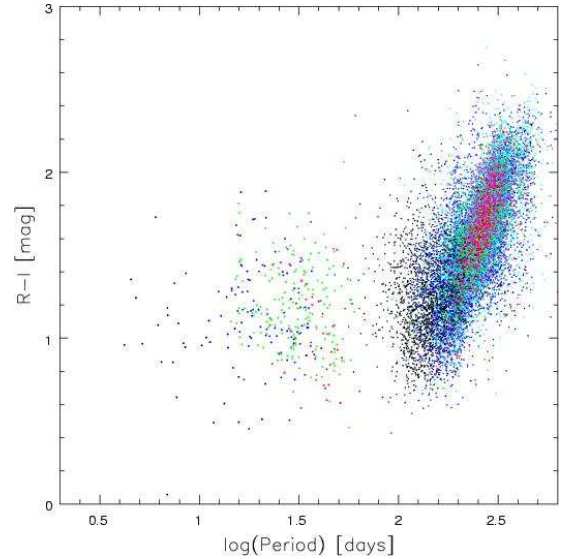

Fig. 23. This figure shows the variation color $R - I$ as function of the period of the variable sources. The color coding is the same as in Figs. 15 and 22. Note, that due to the normalization to the fluxes of Vega in the particular system this $R - I$ color has not to be mistaken with the color of the variation amplitudes of the sources. Nevertheless, some trends are visible in this diagram: As the variation of the LPVs gets redder with increasing period, the I-band periods become more significant, reflecting the rising S/N in I due to higher $R - I$ values and a rising regularity of the light curves.

regular variables. Group III consists of 4287 irregular and 18974 regular/semi-regular variables. 82 presumably group III members show variations on timescales longer than the survey length. The positions in the R-band period-amplitude plane of the 31 eclipsing binary candidates coincide with the positions of groups I and II. Finally we detect 39 miscellaneous variables, among them 16 novae and 15 R Coronae Borealis candidates.

The full catalog is available in electronic form at CDS. We give the name, the position in the WCS, the periods (if available) derived from the R- and I-band data, the amplitudes of the variation ΔF_R and ΔF_I, and provide a classification according to Secs. 4 and 5: DC (classical or δ-Cepheids), SC (s-Cepheids), BC (beat Cepheids), IC (intermediate Cepheids), W (type II Cepheids), RV (RV Tauri stars), S (regular or and semi-regular variations), and I (irregular variables). We also mark the identified Novae (N), eclipsing binary candidates (E), RCB candidates (RCB) and other miscellaneous variables (M). As an illustration of its content we list in Table 2 the entries 100 $-$ 120 in the catalogue. In Figs. 24 to 32 we show typical light curves for each of the groups.

7. Correlation with other catalogues

We cross-correlate our $R-$band selected catalogue with the General Catalogue of Variable Stars (GCVS,

Id	$\alpha(2000.0)$	$\delta(2000.0)$	P_R[days]	$-\log(s_R)$	P_I[days]	$-\log(s_I)$	ΔF_R	ΔF_I	Type
WeCAPP_V00100	0h42m18.46s	41d08′09.0″	119.70	13.18	122.10	8.52	0.37	1.06	I
WeCAPP_V00101	0h42m09.65s	41d08′08.1″	274.99	21.65	277.50	26.10	0.78	2.86	S
WeCAPP_V00102	0h42m31.76s	41d08′11.5″	500.40	9.60	478.70	22.69	0.47	3.48	S
WeCAPP_V00103	0h42m20.06s	41d08′04.4″	180.79	29.32	180.21	26.71	0.76	1.70	S
WeCAPP_V00104	0h42m31.53s	41d08′08.1″	289.96	18.52	293.51	23.71	0.74	3.18	S
WeCAPP_V00105	0h42m52.12s	41d08′11.0″	299.24	33.60	302.18	41.93	0.63	2.59	S
WeCAPP_V00106	0h43m17.73s	41d08′12.8″	136.3	8.920	140.74	4.86	0.49	1.05	I
WeCAPP_V00107	0h42m19.93s	41d08′09.7″	284.59	10.99	273.54	29.43	0.43	2.03	S
WeCAPP_V00108	0h42m45.51s	41d08′10.7″	268.01	19.64	267.94	38.87	0.57	2.56	S
WeCAPP_V00109	0h42m18.84s	41d08′08.8″	240.35	21.15	247.07	27.50	0.51	1.74	S
WeCAPP_V00110	0h42m17.75s	41d08′08.8″	423.96	5.730	423.96	24.32	0.48	1.36	S
WeCAPP_V00111	0h42m17.43s	41d08′08.6″	280.04	16.27	278.51	27.95	0.48	1.69	S
WeCAPP_V00112	0h42m30.69s	41d08′07.9″	216.48	17.07	218.03	21.92	0.81	2.21	S
WeCAPP_V00113	0h42m17.04s	41d08′06.8″	229.50	25.36	229.51	28.31	0.79	2.58	S
WeCAPP_V00114	0h43m02.66s	41d08′13.0″	226.44	29.33	230.99	35.27	0.53	1.96	S
WeCAPP_V00115	0h42m35.32s	41d08′12.0″	-	-	-	-	-	-	L
WeCAPP_V00116	0h42m23.24s	41d08′11.1″	314.68	24.78	319.13	31.99	0.53	2.60	S
WeCAPP_V00117	0h42m14.70s	41d08′10.1″	214.96	26.14	209.84	27.26	0.59	1.77	S
WeCAPP_V00118	0h42m24.75s	41d08′12.4″	277.49	10.20	280.04	23.22	0.42	1.53	S
WeCAPP_V00119	0h42m47.43s	41d08′11.0″	497.12	24.86	505.28	28.47	0.80	6.19	S
WeCAPP_V00120	0h42m24.29s	41d08′11.5″	198.21	21.46	198.61	23.74	0.46	2.82	S

Table 2. Extract from the WeCAPP catalogue of variable stars. We give the identification, the right ascension and declination, the assigned period and its significance s ($0.1 \triangleq$ un-significant, $70 \triangleq$ highly significant) in R and I, the amplitude of variation in both bands, and finally a classification according to the scheme presented in Secs. 4 and 5. The variation amplitudes ΔF_R and ΔF_I are given in units of $[10^{-5}$ Jy].
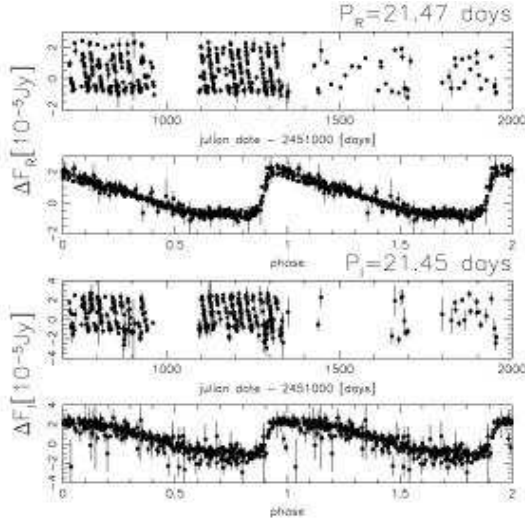

Fig. 24. Light curve of a δ-Cepheid (group I) in the R-band (top panels) and the I-band (bottom panels). In the upper panels we show the light curve R-band, the lower panels show the light curves in the I-band. In both bands the light curves are presented in the time domain (top for each band) and and in the phase domain, i.e. convolved with the derived periods (bottom for each band). Additionally we show the periods P_R and P_I derived in the R- and I-band, respectively.
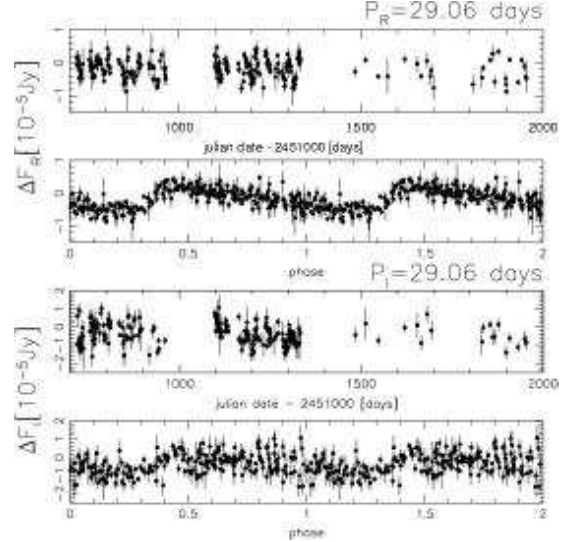
Durlevich et al. (1996)) and catalogues selected in the X-ray (Chandra; Kaaret (2002) & Kong et al. (2002)).

Fig. 25. Light curve of a long period type II Cepheid (group II) in the R-band (top panels) and the I-band (bottom panels).

We find 23 coincidences with the Kaaret (2002) catalogue when using a search radius of $1''$. To estimate how many coincidences we expect by chance we follow the approach proposed by Hornschemeier et al. (2001). We shift one of the catalogues to be compared (in our case we shift the catalogues taken from the literature) by $20''$ in northeast, south-east, south-west and north-west direction, and check for coincidences between these mock catalogues and

WeCAPP	α(2000)	δ(2000)	Kaaret	2MASS	Δ r(arcsec)
10578	0h42m10.30s	41d15'10.4''	J004210.2+411510	0042102+411510	0.5
16262	0h42m12.14s	41d17'58.8''	J004212.1+411758	0042121+411758	0.4
8624	0h42m18.68s	41d14'01.8''	J004218.6+411402	0042186+411402	0.5
8946	0h42m21.58s	41d14'19.8''	J004221.5+411419	0042215+411419	0.4
7582	0h42m25.11s	41d13'40.7''	J004225.1+411340		0.6
19068	0h42m31.26s	41d19'38.7''	J004231.2+411938	0042312+411938	0.2
7979	0h42m36.59s	41d13'49.9''	J004236.6+411350		0.7
9082	0h42m39.60s	41d14'28.6''	J004239.5+411428		0.9
11406	0h42m41.45s	41d15'23.9''	J004241.4+411524		0.3
16322	0h42m43.97s	41d17'55.5''	J004243.9+411755		0.4
15344	0h42m44.88s	41d17'39.5''	J004244.8+411740		0.4
12503	0h42m46.99s	41d16'15.3''	J004246.9+411615		0.7
8501	0h42m47.13s	41d14'13.9''	J004247.1+411413		0.8
10431	0h42m47.45s	41d15'07.6''	J004247.4+411507		0.2
11736	0h42m47.90s	41d15'50.6''	J004247.8+411550		0.6
12891	0h42m48.65s	41d16'25.0''	J004248.6+411624		0.7
20170	0h42m55.27s	41d20'45.1''	J004255.3+412045		0.7
18374	0h42m59.66s	41d19'19.3''	J004259.6+411919		0.3
12404	0h42m59.88s	41d16'06.0''	J004259.8+411606		0.1
21059	0h43m03.31s	41d21'21.8''	J004303.2+412121		0.5
6049	0h43m08.42s	41d12'46.9''	J004308.4+411247		0.7
8360	0h43m09.88s	41d19'00.8''	J004309.8+411900		0.7
9991	0h43m10.62s	41d14'51.3''	J004310.5+411451	0043106+411451	0.5

Table 3. Coincidences between the WeCAPP catalogue of variable stars and the X-ray selected catalogue of point sources by Kaaret (2002). A search radius of 1'' was used. We give the identifier and WCS coordinates for the WeCAPP sources, and the identifier for the Kaaret (2002) sources. For sources coincident with the 2MASS catalogue (Cutri et al., 2000) we give the 2MASS identifier also. Additionally we show for each of the correlated sources the difference Δ r of the matching of both catalogues. Source WeCAPP_V10431 is identical with the (dwarf-)nova WeCAPP-N2000-05 which shows supersoft X-ray emission (Pietsch et al., 2005).
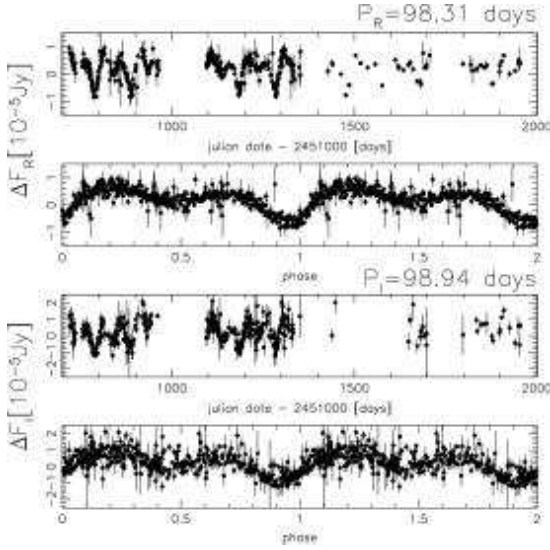

Fig. 26. Light curve of a RV Tauri star (group II) in the R-band (top panels) and the I-band (bottom panels). We show the light curves convolved with the formal periods (deep minimum to deep minimum). The double wave light curve with alternating deep and shallow minima is nicely uncovered.
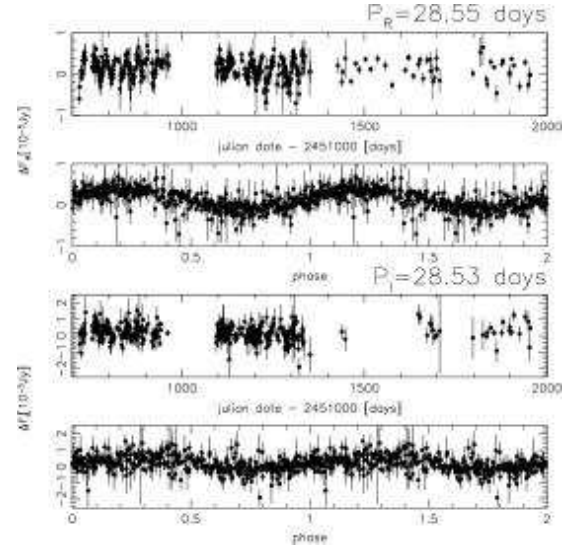

Fig. 27. Light curve of a low period semi-regular variable (group II) in the R-band (top panels) and the I-band (bottom panels).

our catalogue. By averaging these numbers we get the expected number of coincidences by chance.

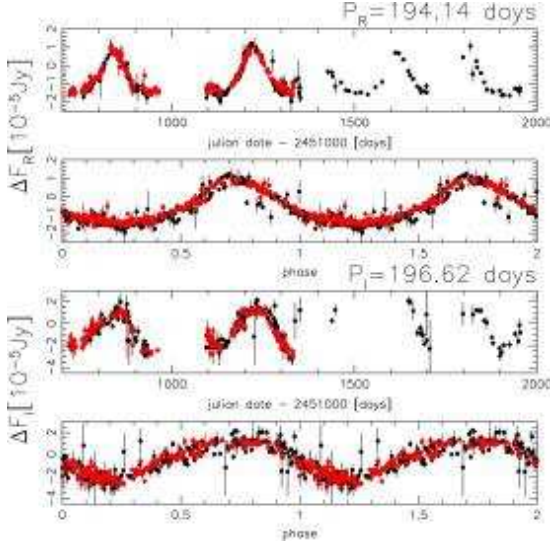Applying a search radius of 1'' the number of false coincidences with the Kaaret (2002) catalogue becomes 12.

Fig. 28. Light curve of a LPV with regular variation (group III) in the *R*-band (top panels) and the *I*-band (bottom panels). As illustration of the agreement of the data taken with different telescopes we show the data collected at Calar Alto as red dots, and data taken at Wendelstein as black dots.
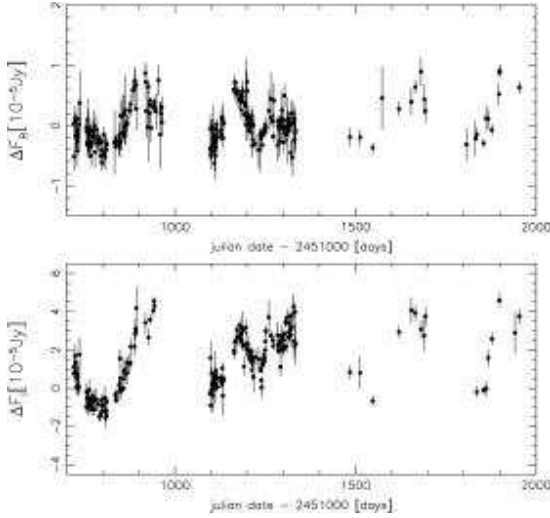

Fig. 29. Light curve of an irregular LPV (group III). Top panel: *R*-band. Bottom panel: *I*-band.

Fig. 30. Light curve of a LPV (group III) with changing variation amplitudes from cycle to cycle. Top panels: *R*-band. Bottom panels: *I*-band.

Fig. 31. Light curve of a R Coronae Borealis candidate (miscellaneous variables). Top panel: *R*-band. Bottom panel: *I*-band. These rare carbon-rich stars show unpredictable and frequent fading of light in optical wavebands, most probably due to dust grains ejected from the stellar photosphere. For a review on these RCB stars see Clayton (1996).

This high level of false coincidences (about 50%) results from the high number density of the variable star catalogue. Nevertheless, the false detections rate suggests that about 11 of the coincidences should be real. This is supported by the fact, that 6 of the coincident sources have an entry in the 2 MASS catalogue (Cutri et al., 2000), 8 of the Kaaret-WeCAPP sources are identified as globular clusters (4 of them with a 2MASS entry, Kaaret (2002)). Furthermore we find that 12 of the sources have coincident counterparts in the Kong et al. (2002) catalogue as well (see below). In Table 3 we give the positions of all 23
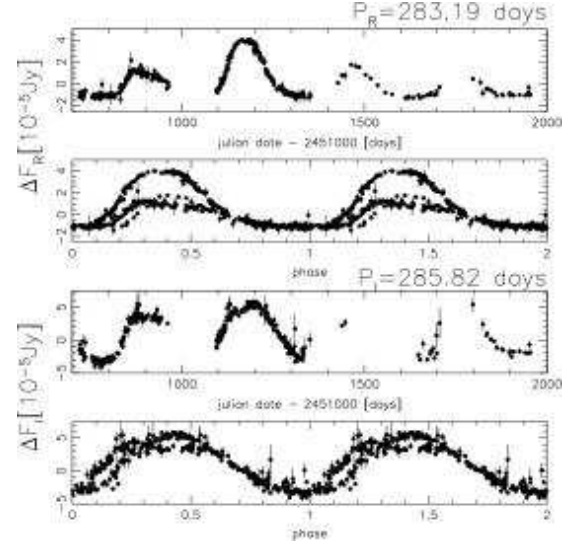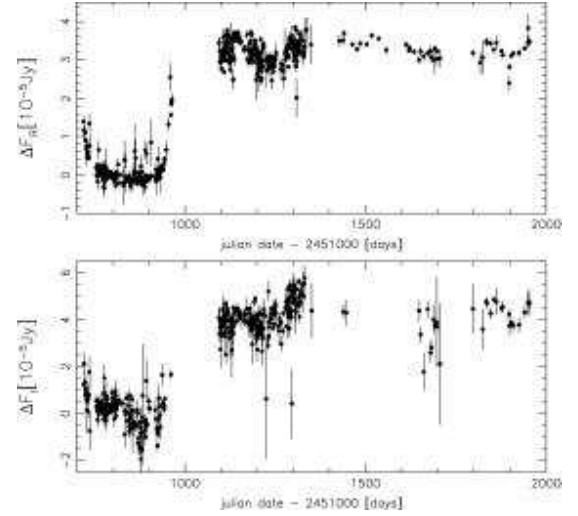
coincidences, for sources with entries in the 2MASS catalogue we give the 2MASS name also. Two of the Kaaret-WeCAPP sources with 2MASS fluxes (WeCAPP_V8946 and WeCAPP_V10578) have no globular cluster (gc) counterpart (Kaaret, 2002). Whereas V8946 coincides with a gc-candidate identified by Wirth, Smarr, & Bruno (1985) a gc-counterpart for WeCAPP_V10578 is completely unknown.

WeCAPP	$\alpha(2000)$	$\delta(2000)$	Kong et al.	Δ r(arcsec)
14906	0h42m07.08s	41d17′20.2″	J004207.0+411719	0.9
15982	0h42m09.49s	41d17′45.6″	J004209.4+411745	0.7
16262	0h42m12.14s	41d17′58.8″	J004212.1+411758	0.8
5801	0h42m15.09s	41d12′34.8″	J004215.0+411234	0.6
14846	0h42m15.65s	41d17′21.9″	J004215.6+411721	0.7
12198	0h42m16.06s	41d15′53.3″	J004216.0+411552	0.4
7582	0h42m25.11s	41d13′40.7″	J004225.1+411340	0.3
20282	0h42m27.61s	41d20′49.0″	J004227.6+412048	0.3
13905	0h42m30.23s	41d16′54.3″	J004230.2+411653	0.9
19068	0h42m31.26s	41d19′38.7″	J004231.2+411939	0.7
11863	0h42m32.51s	41d15′45.7″	J004232.5+411545	0.2
10895	0h42m34.76s	41d15′22.9″	J004234.7+411523	0.3
7979	0h42m36.59s	41d13′49.9″	J004236.5+411350	0.3
11406	0h42m41.45s	41d15′23.9″	J004241.4+411523	0.3
10626	0h42m43.74s	41d15′14.4″	J004243.7+411514	0.8
15344	0h42m44.88s	41d17′39.5″	J004244.8+411739	0.3
15318	0h42m46.12s	41d17′36.3″	J004246.0+411736	0.8
12503	0h42m46.99s	41d16′15.3″	J004246.9+411615	0.6
11736	0h42m47.90s	41d15′50.6″	J004247.8+411549	0.8
22406	0h42m48.94s	41d24′06.1″	J004248.9+412406	1.0
17309	0h42m56.93s	41d18′44.4″	J004256.9+411844	0.2
18374	0h42m59.66s	41d19′19.3″	J004259.6+411919	0.4
12404	0h42m59.88s	41d16′06.0″	J004259.8+411606	0.2
15035	0h43m01.80s	41d17′26.5″	J004301.8+411726	0.5
10871	0h43m02.99s	41d15′22.3″	J004302.9+411522	0.6
21059	0h43m03.31s	41d21′21.8″	J004303.3+412122	0.6
16325	0h43m03.90s	41d18′04.7″	J004303.8+411805	0.5
19890	0h43m07.55s	41d20′20.0″	J004307.5+412020	0.1
17815	0h43m09.88s	41d19′00.8″	J004309.8+411901	0.4
9991	0h43m10.62s	41d14′51.3″	J004310.6+411451	0.8
17140	0h43m16.14s	41d18′41.5″	J004316.1+411841	0.6

Table 4. Coincidences between the WeCAPP catalogue of variable stars and the X-ray selected catalogue of point sources by Kong et al. (2002). A search radius of 1″ was used. We give the identifier and WCS coordinates for the WeCAPP sources, and the identifier for the Kong et al. (2002) sources. Additionally we show for each of the correlated sources the difference Δ r of the matching of both catalogues. The position of the beat Cepheid candidate WeCAPP_15035 coincides with the X-ray source J004301.8+411726.

The Kong et al. (2002) catalogue contains 31 coincidences with our variable star catalogue when applying a 1″ search radius. As we expect 17 coincidences by chance about 14 of the coincidences should be real. As mentioned above 12 of the sources are also coincident with the Kaaret (2002) catalogue. We show the position of all 31 coincidences in Table 4.

The GCVS (Durlevich et al., 1996) comprises 250 entries within our field of view, most of them being of nova type. 161 (6) were classified as novae, additionally 53 as novae of fast type (NA), 9 (2) of slow type (NB), and (2) of very slow type (NC). Furthermore the GCVS reports 1 SNIa remnant in our field, 1 (1) LC type (irregular variable supergiant), 3 (1) semi-regular variables (SR), 3 δ-Cepheids, (1) SDOR variable, 2 (1+2) irregular variables, and 1 unstudied (S: classification) variable. The numbers in brackets give additional candidates for the particular variable star group with questionable classifications according to the GCVS.

The crowding of the WeCAPP sources demands that we keep the search radius at 1″, even when comparing with the GCVS, whose accuracy is well below this value. We find 27 coincidences, the number of false detections (21) suggests however, that most of the coincidences are not real. As furthermore 23 of them are classified as novae in the GCVS we only show the 4 coincidences which we regard as real in Table 5. Note, that we do not match the positions of all three δ-Cepheids found in the GCVS inside our field. The GCVS Cepheid V0934 has a position difference of 2.1″ when compared to our position, GCVS Cepheid V0811 is off by 10.2″. Because of these in parts large uncertainties in the positions of the GCVS we are not trying to match the two remaining semi-regulars given their smaller variation amplitude.

8. Conclusions and outlook

We presented the catalogue of variable stars detected by the WeCAPP project in the central parts of M31. The observations in the optical R and I bands towards the bulge

WeCAPP	α(2000)	δ(2000)	GCVS	Δ r(arcsec)	GCVS class	WeCAPP class
906	0h43m22.50s	41d07$'$28.6$''$	V0871	0.7	I:	I
2375	0h43m15.73s	41d07$'$54.7$''$	V0727	0.1	IA:	I
559	0h43m24.16s	41d07$'$12.7$''$	V0743	0.2	DCEP	DC
742	0h43m17.27s	44d15$'$58.0$''$	V0726	1.0	SR	I

Table 5. Coincidences between the WeCAPP catalogue of variable stars and the General Catalogue of Variable Stars (GCVS, Durlevich et al. (1996)). A search radius of $1''$ was used. We give the identifier, WCS coordinates and a classification for the WeCAPP sources, and the identifier and a classification according to the GCVS. Additionally we show for each of the correlated sources the difference Δ r of the matching of both catalogues.
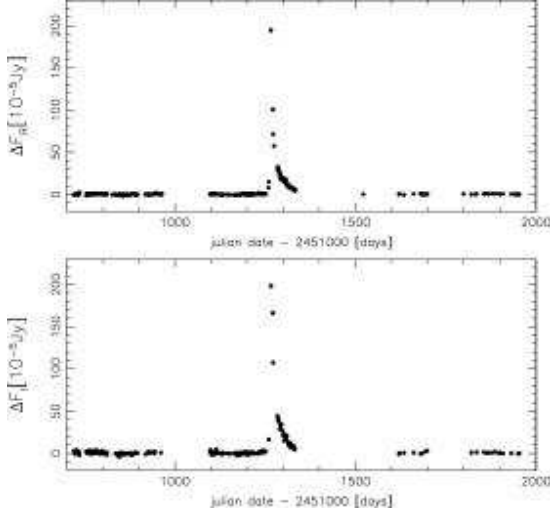

Fig. 32. Light curve of a nova (miscellaneous variables). Top panel: R-band. Bottom panel: I-band. A paper concerning the characteristics of all detected novae is in preparation.

of M31 covering the years 2000-2003 with very good time sampling resulted in a database of over 23000 variable sources. The catalogue containing regular, semi-regular and irregular LPVs, Cepheids, RV Tauri stars, eclipsing binary and R Coronae Borealis candidates enlightens the rich population of variable sources in M31. Two more papers dealing with the Fourier parameters for the Cepheid-like stars and the WeCAPP nova catalogue are in preparation. A fraction of the nova catalogue has already been correlated with supersoft X-ray sources (SSSs) in M31, showing that classical novae constitute the major class of SSSs in M31 (Pietsch et al., 2005).

The distribution of the identified variable sources shows an asymmetry due to the enhanced extinction in the spiral arms projected on the M31 bulge. Assuming that the non-variable stars in the bulge behave in the same way as the variable counterparts this asymmetry enlarges the expected asymmetry in the microlensing signal resulting from the high inclination of M31. Therefore theoretical calculations have to take a modified distribution of sources (or the distribution of the extinction present in a given band) into account.

Recently it was proposed that sequence E, first detected by Wood (1999) in the MACHO data towards the LMC bar, is populated by ellipsoidal red giants (Soszynski et al., 2004). Wood (1999) found five distinct period-luminosity sequences, of which three could be attributed to different evolutionary phases and pulsation modes. For two of them, the sequences D and E, it was suggested that they are populated by contact binaries, and semi-detached binaries with an invisible companion. Analyzing the data of the LMC ellipsoidal candidates from the OGLE web archive[4] and accounting for the distance modulus of M31 proves that these sources are below the detection limit of our survey. Therefore, we can not put any constraints on a possible population of ellipsoidal red giants in M31.

The more detailed examination of the group III LPVs will be subject to future work. Until now we measured the dominant period in these stars which are known to show multi-periodic phenomena. Future work will include the extraction of the sub-dominant periods and the distribution of the ratio of the different periods. Furthermore, the distribution and possible correlations of the Fourier parameters for these stars is an interesting and until now unstudied problem which we can address with this dataset.

References

Alard, C. & Lupton, R. 1998, ApJ, 503, 325

Alard, C. 1999, A&A, 343, 10

Alard, C. 2000, A&AS, 144, 363

Alcock, C., Allsman, R.A., Axelrod, T.S., et al. 1995, AJ, 109, 1653

Alcock, C., Allsman, R.A., Alves, D.R., et al. 1998, AJ, 115, 1921

Alcock, C., Allsman, R.A., Axelrod, T.S., et al. 1999, ApJ, 511, 185

---

[4] http://ogle.astrouw.edu.pl/

An, J.H., Evans, N.W., Hewett, P. et al. 2004, MNRAS, 351, 1071

Ansari, R., Auriere, M., Baillon, P. et al. 1997, A&A, 324, 843

Ansari, R., Auriere, M., Baillon, P. et al. 2004, A&A, 421, 509

Antonello, E. & Poretti E., 1986, A&A, 169, 149

Auriere, M., Baillon, P., Bouquet, A. et al. 2001, ApJ, 553, 137

Baade, W. & Swope, H.H., 1963, AJ, 68, 435

Baade, W. & Swope, H.H., 1965, AJ, 70, 212

Beaulieu, J.P., Grison, P., Tobin, W. et al. 1995, A&A, 303, 137

Beaulieu, J.P., Krockenberger, M., Sasselov, D.D. et al., 1997, A&A, 321, L5

Bessell, M. S., PASP91, 589

Bertin, E. & Arnouts, S., 1996, A&AS, 117, 393

Binney, J. & Merrifield, M. 1988, in Galactic Astronomy, Princeton Series in Astrophysics

Calchi Novati, S., Iovane, G., Marino, A.A. et al. 2002, A&A, 381, 848

Cassisi, S., Castellani, V., degl'Innocenti, S., Weiss, A. 1998 , A&AS,129, 267

Cieslinski, D., Diaz, M.P., Mennickent, R.E. & Pietrzynski, G. 2003, PASP, 115, 193

Clayton, G. C. 1996, PASP, 108, 225

Cutri, R. M. et al., *Explanatory Supplement to the 2MASS Second Incremental Data Release*

de Jong, J.T.A., Kuijken, K., Crotts, A.P.S. et al. 2004, A&A, 417, 461

Derue, F., Marquette, J.-B., Lupone, S. et al. 2002, A&A, 389, 149

Durlevich, O., Kazarovets, E., Kholopov, P., Kireeva, N., Samus, N., & Tsvetkova 1996, in: The General Catalogue of Variable Stars, fourth edition (as available from the CDS)

Feast, M. W., Glass, I.S., Whitelock P., & Catchpole, R. M., 1989, MNRAS, 241, 375

Feast, M. W., Whitelock, P. & Menzies, J., 2002, MNRAS, 329, L7

Fokin, A. B. 2001, in Stellar Pulsation-Nonlinear Studies,(eds.) Takeuti M. & Sasselov D.D. 2001, 103, Kluwer Academic Publishers

Gössl, C.A. & Riffeser, A. 2002, A&A, 381, 1095

Grillmair, C. J., Lauer, T. R., Worthey, G. et al. 1996, AJ, 112, 1975

Haiman, Z.,et al., 1994, A&A, 286, 725

Hertzsprung, E., 1924, BAN, 3, 115

Horne, J.H. & Baliunas, S.L. 1986, ApJ, 302, 757

Hornschemeier, A.E., et al. 2001, ApJ, 554, 742

Hubble, E.P. 1922, ApJ 56, 162

Iben, I. & Renzini, A., 1983, ARAA, 21, 271

Jablonka, P., Bridges, T.J., Sarajedini, A., et al. 1999, ApJ, 518, 627

Lebzelter T., Schultheis M., & Melchior A.L. 2002, A&A, 393, 573

Lomb, N.R., 1976, Astrophysics and Space Science, 39, 447

Kaaret, P. 2002, ApJ, 578, 114

Kaluzny, J., Stanek, K.Z., Krockenberger, M. et al. 1998, AJ, 115,1016

Kent, S. 1989, AJ, 97, 1614

Kong, A.K.H., Garcia, M.R., Primini F.A. et al., 2002, ApJ, 577, 738

Kovacs, G., Zucker, S., & Mazeh, T., 2002, A&A, 391, 369

Kwee, K.K., Bull. Astron. Inst. Netherlands, 19, 260

Magnier, E.A., Lewin, W.H.G., van Paradijs, J. et al. 1992, A&AS, 96, 379

Noda, S., Takeuti, M., Abe, F. et al. 2002, MNRAS, 330, 137

Noda, S., Takeuti, M., Abe, F. et al. 2004, MNRAS, 348, 1120

Maraston, C. 1998, MNRAS, 300, 872

Massey, P., Hodge, P. W., Holmes, S., Jacoby, G., King, N. L., Olsen, K., Saha, A., and Smith, C. AAS 199th meeting, Washington, DC, January 2002, 130.05

Pietsch, W., Fliri, J., Freyberg, M.J. et al., 2005, A&A, in press, astro-ph/0504321

Press W.H., Teukolsky S.A., Vetterling W.T., Flannery B.P. 1988, Numerical Recipes, Cambridge University Press

Rejkuba, M., Minniti, D., Silva, D.R. & Bedding, T.R. 2003, A&A, 411, 351

Renzini, A. 1998, AJ, 115, 2459

Riffeser, A., Fliri, J., Gössl, C.A. et al. 2001, A&A, 379, 362

Riffeser, A., Fliri, J., Bender, R., Seitz, S., Gössl, C.A. 2003, ApJ, 599, L17

Riffeser, A., Fliri, J., & Gössl, C.A., in prep.

Roberts D.H., Lehar J., & Dreher J.W. 1987, AJ, 93, 968

Scargle, J.D., 1982, ApJ, 263, 835

Simon, N.R. & Lee A., 1981, ApJ, 248, 291

Simon, N.R. & Moffett T.J., 1986, PASP, 97, 1078

Soszynski, I. Udalski, A., Kubiak, M. et al., 2004, Acta, 54, 347

Szymanski, M., Kubiak, M., & Udalski, A., 2001, Acta, 51, 259

Stanek, K.Z. & Garnavich, P.M. 1998, ApJ, 503, 131

Tingley, B., 2003, A&A, 408, L5

Wallerstein G., PASP, 111, 689

Whitelock, P., Marang, F., & Feast, M., 2000, MNRAS, 319, 728

Wirth, A., Smarr, L.L., & Bruno, T.L., 1985, ApJ, 290, 140

Wood, P.R., 1999, IAUS, 191, 151

Wood, P.R., 2000, PASA, 17, 18

Wray, J.J., Eyer L. & Paczynski B. 2004, MNRAS, 349, 1059

Appendix A: Survey window function and leakage function

Effects induced by the discrete time sampling of astronomical surveys can yield strong power in frequencies not caused by a periodic or quasi-periodic signal. The frequen-

cies affected are often connected to the daily separation of observations or to observing blocks interrupted yearly by the non-observability of the object. In case of M31 the observation gap usually lasts from the mid of March to the beginning of June.

A quantitative way to describe the effects of the time sampling of the observations on the power spectrum is given by the window function $W(\nu)$. $W(\nu)$ is defined as the Fourier transform of the sampling function $s(t)$, where $s(t_i)$ is of constant value in case of observations taking place at times t_i and zero otherwise:

$$W(\nu) = \int s(t)\, e^{-2\pi i \nu t} dt \ . \tag{A.1}$$

In Figs. A.1 and A.2 we show the window function $W(\nu)$ (in the frequency and period representation, respectively) calculated with the Lomb algorithm for the sampling given in Field F1. For this purpose we created a high (order of 10^{14}) signal-to-noise-ratio (S/N) light curve with $s(t_i) = 1 + \sigma(t_i)$ and a minimal noise contribution $\sigma(t_i)$ to allow for the calculation of the variance of the data (see Eqs. 1 and 3).

Clearly visible is the strong power in periods around 450 days (at $\nu = 2.2 \times 10^{-3}$ days^{-1}), whereas at small periods (high frequencies) no 'aliasing' problem is expected. The full width half maximum ν_{FWHM} of the main peak of the window function $W(\nu)$ determines the theoretical error in the period calculation

$$\Delta P \approx \frac{\Delta \nu}{2} P^2 \tag{A.2}$$

with $\Delta \nu = \nu_{\mathrm{FWHM}}$. According to Roberts et al. (1987) $\Delta \nu$ can be approximated by $\Delta \nu \approx 1/T$ with T the total time span of the observations if the sampling is not to non-uniform. The measured $\nu_{\mathrm{FWHM}} = 0.0013$ day^{-1} is 1.60 times larger than this theoretical value which can be explained by the non-uniform sampling of the observations (see Fig. 2). With this value Eq. A.2 becomes

$$\Delta P \approx 6.5 \times \left(\frac{P}{100\,\mathrm{d}} \right)^2 \ . \tag{A.3}$$

An alternative way to illustrate the sampling effect is given by the 'leakage function' for different periodic signals. The function describes how a signal which is located at zero offset 'leaks' into neighboring frequencies. Figure A.3 shows the leakage function for a periodic signal of the form

$$h_j = 10^{\sin(2\pi(t_i - t_0)/P)} \tag{A.4}$$

calculated with the Lomb algorithm for the sampling $s(t_i)$ of field F1 and different periods P. The problem of high amplitudes in the power spectrum for frequencies corresponding to periods in the range between 350 and 550 days is apparent in this figure also.

In Fig. A.4 we show the leakage function in the period representation. For periods between about 350 and 550
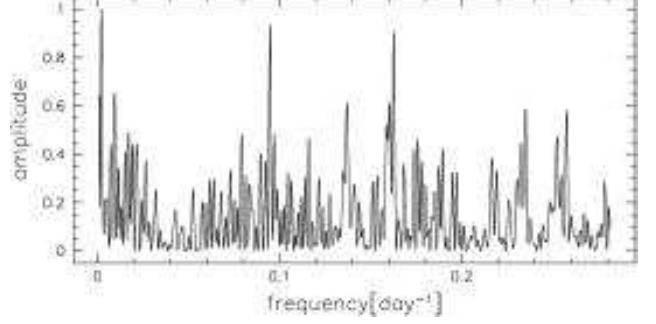

Fig. A.1. This figure shows the window function $W(\nu)$ present in the survey, the amplitude is normalized to 1. $W(\nu)$ is defined as the Fourier transform of the sampling function s(t), $W(\nu) = \int s(t)\, e^{-2\pi i \nu t} dt$. The main peak of the window function has a full width half maximum $\nu_{FWHM} = 0.0013$ day^{-1} which is 1.60 times larger than what one would expect from the total duration of the observations (Roberts et al., 1987).
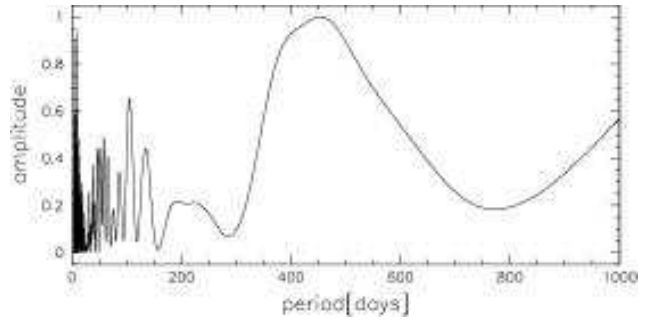

Fig. A.2. Window function $W(\nu)$ shown in the period representation. Clearly visible is the sampling induced strong power in periods around 450 days which give rise to the aliasing problems (see also Figs. A.3 and A.4).

days the power in the second peak in the Fourier spectrum can exceed the power in the first peak which means that the derived period is offset from the real one by the position of the second peak.

Appendix B: Monte Carlo simulation

Additionally we tested the accuracy of the period determination with Monte Carlo simulations of the survey. We look for the dependence of the accuracy for different mean magnitudes and amplitudes at a fixed position, hence fixed noise contributions of the galaxy and the sky. We choose the mean magnitude M_R of the variable to be $M_R = -1, 0, 1, 2$ mag and shift them to the distance of M31. For each of these mean magnitudes we change the amplitude A_R of the variation from 0.5 mag to 2 mag. The background (surface brightness of the galaxy + sky contribution) is set to $M_{bg,R} = 19$ mag per area of the PSF. In each run we simulate 10^5 light curves according to

$$F_R(t_i) = 10^{-0.4(M_R + (m_R - M_R) + A_R \sin(2\pi(t_i - t_0)/P_{in}))} \ . \tag{B.1}$$
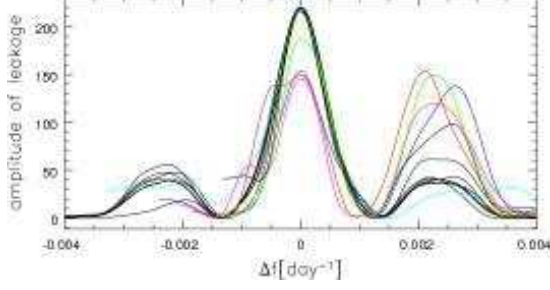
Fig. A.3. Leakage function for the sampling given in the survey for different periodic signals. The function shows how a signal which is located at zero offset leaks into neighboring frequencies. We calculated this function for a signal according to Eq. (A.4) and periods of 5, 10, 20, 50, 100, 200, 250, 300 (cyan curve), 400, 450, 500, 550, 600, and 700 days (black curves, if not mentioned otherwise). The power in the second peak is high for periods of 400 (blue curve), 450 (magenta curve), and 500 days (red curve). In this period regime the power in the second peak can exceed the power in the first peak (at zero frequency difference) resulting in an aliasing of periods. The aliasing problem gets lower for periods of 550 (green curve) and 600 days (yellow curve), and vanishes for even larger periods. The aliasing problem is also evident in the Monte-Carlo simulation of the survey.
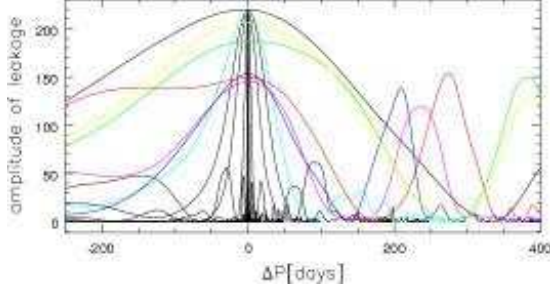

Fig. A.4. Leakage function in the period representation for the sampling given in the survey for different periodic signals. Color coding as in Fig.A.3. For periods between 350 and about 550 days the power in the second peak can exceed the power in the first peak (at zero period difference) resulting in a possible aliasing of periods. The resulting displacement of the true period can be read from the x-axis.

The epochs t_i are given by the sampling of field F1 (see Fig. 2), periods P_{in} are chosen randomly between 3 and 700 days, and t_0, the epoch of mean luminosity is randomly distributed between the beginning and the end of the survey. Note, that this also ensures that the phase is randomly chosen. For each simulated light curve the period is derived according to Eq. 1. Figure B.1 shows the derived periods P_{out} as a function of the input period. It is clearly seen that the accuracy of the period determination decreases at around 500 days, independently of the S/N of the light curves. This can partly be explained by the sparse time sampling in the last two campaigns. On the

other hand also aliasing effects due to the yearly observing window seem to play a role for periods between 350 days and 550 days (see Figs. A.3, A.4 and B.1). This holds for S/N-ratios above a certain threshold. Noise present in the light curves tends to level out the different peaks in the power spectrum which results in a generally bad performance of the period determination for light curves with low S/N. For higher S/N light curves the accuracy of the period determination is good apart from the problem that periods around 400 and 500 days tend to be shifted to much smaller (i.e. around half of the true) values.
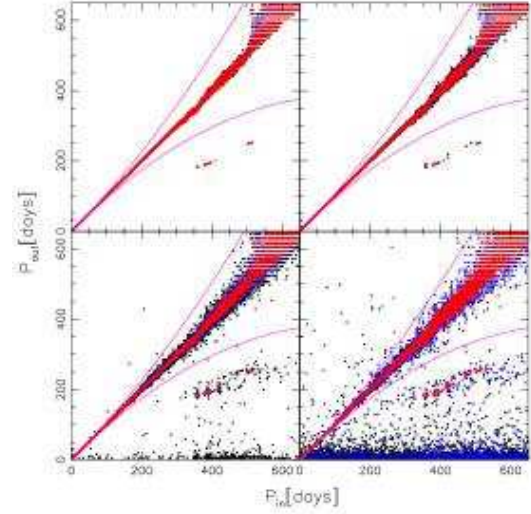

Fig. B.1. Result of simulations for decreasing S/N of the light curves from the upper left to the lower right corner. The mean magnitude of the source changes in steps of one magnitude from $M_R = -1$ mag in the upper left corner to $M_R = 2$ mag in the lower right corner. Red dots show the accuracy of the period determination for light curves with an amplitude $A_R = 2.0$ mag, blue dots correspond to $A_R = 1.0$ mag, and black dots have $A_R = 0.5$ mag. The apparent horizontal lines at large periods result from the finite frequency resolution of the period finding algorithm. Above a threshold in S/N the accuracy of the period determination seems independent of the particular S/N of the light curves. In this regime only periods larger than 500 days have a large false detection probability. Below the threshold the accuracy breaks down very rapidly, independent of the period. In magenta we show the theoretical expected errors of the period determination according to Eq. A.3.